R. & M. No. 3390

MINISTRY OF AVIATION

AERONAUTICAL RESEARCH COUNCIL
REPORTS AND MEMORANDA

Measurements at Subsonic and Supersonic Speeds of the Longitudinal and Lateral Stability of a Slender Cambered Ogee Wing Including the Effects of a Fin, Canopy Nose and Trailing-Edge Controls

By D. Isaacs

LONDON: HER MAJESTY'S STATIONERY OFFICE
1965
PRICE £1 6s. 0d. NET

Measurements at Subsonic and Supersonic Speeds of the Longitudinal and Lateral Stability of a Slender Cambered Ogee Wing Including the Effects of a Fin, Canopy Nose and Trailing-Edge Controls

By D. Isaacs

Communicated by the Deputy Controller Aircraft (Research and Development), Ministry of Aviation

*Reports and Memoranda No. 3390**

September, 1963

Summary.

The results show that for longitudinal stability at $M = 0{\cdot}3$ and $C_L = 0{\cdot}45$, the centre of gravity of an actual aircraft could be located only forward of 45% $\bar{c}$ (66% c_0). The centre of pressure of the wing with basic nose and no fin is at 53% $\bar{c}$ (71% c_0) at the cruise attitude, $M = 2{\cdot}2$ and $C_L = 0{\cdot}075$, so that the camber used is insufficient to trim the wing. Measured values of the drag increments due to control deflection show fair agreement with linear-theory estimates. The control effectiveness ($dC_L/d\eta_c$, $dC_m/d\eta_c$ and $dC_l/d\xi_c$) can be predicted with fair accuracy. The canopy nose is slightly de-stabilizing in yaw, and it has a drag penalty which is probably larger than could be tolerated (30% of basic wing wave drag). At supersonic speeds slender-body theory is generally inadequate for predicting the lateral derivatives of the wing. The fin effectiveness (except on l_v) can be estimated with good accuracy.

LIST OF CONTENTS

* Replaces R.A.E. Report No. Aero. 2679—A.R.C. 25 598.

LIST OF CONTENTS—*continued*

LIST OF APPENDICES

LIST OF TABLES

LIST OF ILLUSTRATIONS

LIST OF ILLUSTRATIONS—*continued*

Figure

Figure

---

1. *Introduction.*

As part of the programme to investigate wing shapes suitable for supersonic transport aircraft, extensive wind-tunnel testing has been undertaken on a wide range of wings in order to determine the capabilities of present theoretical design methods. The tests reported here are concerned with the problem of trimming an aircraft in supersonic flight both by a particular camber design and by deflection of trailing-edge controls, but include measurements of longitudinal and lateral static stability derivatives for the wing. In addition the effects of adding both a canopy at the nose and rear stabilizing fin are studied.

For a plane wing of the type of ogee planform considered the aerodynamic centre (and centre of pressure) moves aft some 5 to 10% of aerodynamic chord with increase of Mach number from subsonic to supersonic. Hence a plane wing which is statically stable longitudinally at low speeds is untrimmed at supersonic speeds. The centre-of-pressure shift can be reduced by the use of camber. The wing tested is one of a series with camber shapes designed using slender-wing theory in the way described by Weber[1]. It is one of a family of four wings, all of which have the same ogee planform and the same spanwise distribution of area in each cross-section. It was designed for a pitching-moment coefficient of 0·00853 at zero C_L, equivalent to a centre-of-pressure shift of 7% c_0 at $C_L = 0{\cdot}075$. Of the four wings, one is plane and the other three (including the one dealt

with in this report) have varying amounts of camber. The longitudinal stability and drag of this family of wings has already been investigated by Taylor[2]. The tests were made in the 8 ft × 8 ft wind tunnel during August and October, 1960.

2. *Experimental Details.*

2.1. *Description of the model.*

The wing (Fig. 1) is of ogee planform with planform parameter $P = 0{\cdot}45$ (P is the ratio of wing area to area of enclosing rectangle). Details of the cross-sectional shape of the wing with the basic nose are shown in Fig. 2. Although this is an integrated shape (no separate fuselage), the volume is distributed in such a way as to provide space for a pressure cabin (Fig. 3).

Since the wing thickness decreases to zero at the trailing edge, it was found necessary to distort the profile over the rear of the wing by the inclusion of a circular-cross-section sting shroud, which is also used as a mounting for the fin.

The variation of the leading-edge sweepback angle along the wing is shown in Fig. 4 and details of the wing camber shape in Figs. 5 to 8. The wing horizontal datum which is used as a reference datum in these figures is also shown in Figs. 1 and 2. It is defined as the plane passing through the wing trailing edge parallel to the free-stream direction with the wing at its design attitude (wing local incidence at trailing edge is zero since design C_L is zero).

On each side of the wing there are two trailing-edge controls, one inboard and one outboard (Fig. 1), the space between them being a possible location for engine nacelles. These controls are of constant chord with the hinge line at 95% c_0. (The wing was designed with no spanwise camber at this section in order to give a straight hinge line.)

The incorporation of a canopy into the nose of the model involves an increase only in the depth of the wing, the planform shape remaining unaltered. The effect of the canopy on the cross-sectional area distribution is shown in Fig. 3, together with the basic wing cross-sectional area distribution, and the effect on this of the fin.

Apart from the noses and fin which were made of epoxy resin and glass fibre on a steel core, the rest of the model was made of steel. All other relevant data about the wing is contained in Tables 1 to 3.

Boundary-layer transition was fixed at the leading edges of the wing and fin by bands of distributed carborundum particles (grade 80), the size of the particles being governed by the requirements at the highest Mach number tested, $M = 2{\cdot}8$. Although no checks on transition were made during these tests, the effectiveness of this size of roughness in producing transition at these Reynolds numbers and Mach numbers has been established during previous testing on slender wings.

2.2. *Test Range.*

The majority of the tests were made at supersonic speeds mainly at $M = 1{\cdot}4$, $1{\cdot}8$, $2{\cdot}2$, $2{\cdot}4$ and $2{\cdot}8$, although a few extra results were obtained at $M = 1{\cdot}6$, $2{\cdot}0$ and $2{\cdot}6$ for the configuration with the basic nose and no fin present. The Reynolds number at all supersonic speeds was 2×10^6 per foot (10^7 based on root chord). In addition, the basic nose configuration with and without fin was tested at subsonic speeds, at $M = 0{\cdot}8$ ($R = 2 \times 10^6$ per foot) and at $M = 0{\cdot}3$ ($R = 2 \times 10^6$

and 8×10^6 per foot). At supersonic speeds and $M = 0{\cdot}8$, measurements were taken over an incidence range of $-4°$ to $+12°$ at sideslip angles of $-2°$ to $+6°$, the incidence range being extended up to 20° at $M = 0{\cdot}3$. The test programme is shown in Table 4.

At most supersonic Mach numbers the tunnel humidity was maintained below the level at which the accuracy of the measurements starts to deteriorate (frost point $\leqslant -30°$). However, for some runs this was impossible and the frost point varied between $-30°$C and $-20°$C. It is thought that the main effect of this increased humidity was to introduce small flow deflections into the airstream. The manner in which the measured results have been corrected for these flow deflections is explained in Section 2·3.

2.3. *Corrections Applied.*

The usual correction has been applied to the drag results to allow for the difference between free-stream and base static pressures.

All measurements made with the model 'upright' have been repeated with it 'inverted', and the results as presented in this report are a mean of these two sets of measurements. In this way the effects on the results of tunnel flow deflections and flow curvature have been eliminated.

Model incidence and sideslip angles have been corrected for sting and balance deflections, and the trailing-edge control setting angles have been corrected for deflection of the hinge plates.

At subsonic speeds the model incidence, drag and pitching-moment coefficients have been corrected for tunnel constraint using the theory of Ref. 3. The corrections for this particular ogee planform are approximately:

$$\frac{\Delta\alpha}{C_L} = 0{\cdot}0100 + \frac{0{\cdot}0026}{\sqrt{(1-M^2)}}$$

$$\frac{\Delta C_m}{C_L} = \frac{0{\cdot}00093}{\sqrt{(1-M^2)}} \left(\frac{dC_L}{d\alpha}\right)_{\text{per radian}}$$

$$\frac{\Delta C_D}{C_L{}^2} = 0{\cdot}0100.$$

A mean value of $dC_L/d\alpha$ was used in the expression for ΔC_m (1·95 per radian both at $M = 0{\cdot}3$ and 0·8). The Mach number and kinetic pressure at $M = 0{\cdot}8$ were corrected for tunnel blockage effects, the increment in Mach number being 0·004.

Except in one or two instances mentioned in the text, the results have *not* been corrected for the presence of the sting shroud. Pressure measurements on the symmetrical version of this wing[2] gave the correction to axial force (the force along the sting-balance axis, positive backwards) at zero lift as:

M	1·4	1·8	2·2	2·4	2·8
ΔC_x	0·00090	0·00065	0·00055	0·00045	0·00035

The estimated corrections to lift and pitching moment due to the asymmetry of the sting shroud are[2]

$$\Delta C_L = 0, \Delta C_m = \frac{0{\cdot}003}{\sqrt{(M^2-1)}}.$$

3. *Presentation of Results.*

All forces have been reduced to coefficient form in the usual way (*see* List of Symbols) and resolved about a stability system of axes*, the moment reference centre being at $0{\cdot}5\ \bar{c}$ (18·476 inches forward of the trailing edge). The tangent definition of incidence α and the sine definition of side-slip β† have been used throughout and unless stated otherwise the model incidence is measured relative to the sting-balance axis (Fig. 5).

As stated in Section 2.3, measurements were made with the model both 'upright' and 'inverted' in order to eliminate the effect of tunnel flow deflections. Shown in Figs. 9 and 10 are plots of typical results (except for the variation of C_m with C_L in Fig. 9 where the changes between upright and inverted are the largest measured). Since the differences between the results of different configurations is sometimes quite small, the experimental points have been omitted from most of the graphs in the interests of clarity. A graphical presentation of results is used throughout, Figs. 11 to 38 dealing with longitudinal stability, drag and control effectiveness and Figs. 39 to 72 with lateral stability and fin effectiveness. Where methods are available the experimental results are compared with theoretical estimates.

4. *Accuracy of Results.*

From consideration of the repeatability of the results, the maximum resolution of the measuring instrumentation and the results obtained by processing 'wind-off' data recorded immediately before and after each Mach number run, the experimental accuracy of the results (mean of upright and inverted) at supersonic speeds is estimated to be:

$$
\begin{aligned}
C_L &\pm 0{\cdot}002 \\
C_m &\pm 0{\cdot}0002 \\
C_D &\pm 0{\cdot}0002 \\
C_Y &\pm 0{\cdot}0005 \\
C_n &\pm 0{\cdot}0002 \\
C_l &\pm 0{\cdot}0002
\end{aligned}
$$

The above figures refer to the absolute accuracy of the results. The accuracy of differences both between different runs and in the same run are probably slightly better than the above. At $M = 0{\cdot}8$ and $M = 0{\cdot}3$ ($R = 8 \times 10^6$ per foot) the above values apply, but at $M = 0{\cdot}3$ ($R = 2 \times 10^6$ per foot) they should be doubled.

The results of an unpublished flow survey show that the Mach number in the tunnel over the region occupied by the model varies from nominal by the following amounts

M Nominal	0·3	0·8	1·4–2·4	2·8
Variation	±0·001	±0·001	±0·005	±0·006

The values of α and β quoted are accurate to $\pm\ 0{\cdot}03°$.

* In a few of the figures dealing with the lateral stability of the wing, body-axes derivatives $l_{v\,B}$ and $n_{v\,B}$ are plotted. It is clearly stated in the text when these are being used.

† Tan α = tan θ cos Φ and sin β = sin θ sin Φ
where θ is the total incidence and Φ is the roll angle measured from the trailing edge horizontal.

5. *Discussion of Results.*

5.1. *Longitudinal Stability and Drag.*

5.1.1. *Wing with basic nose and no fin.*—These results have been analysed in detail in Ref. 2 but for completeness the important points are discussed here. At both subsonic and supersonic speeds the lift-curve slopes are linear at both low and high incidence with a band in between where the variation of C_L with α is non linear (Figs. 11 and 12). The increase in value of $dC_L/d\alpha$ at high incidence due to vortices from wing leading-edge separations, varies from 6% at $M = 2{\cdot}8$ to 30% at $M = 1{\cdot}4$, whereas at subsonic speeds an increase of the order of 80% occurs, although at a higher incidence. The initial lift-curve slope, the incidence $\bar{\alpha}$ at which the increase of slope occurs and the slope for $\alpha > \bar{\alpha}$ are shown in Fig. 15.

At subsonic speeds the pitching-moment curves (Fig. 13) are very non linear with considerable pitch-up occurring as generally found on such wings (*see*, e.g. Spence and Lean[4]). At low supersonic speeds the pitch up is much less pronounced (Fig. 14), but increases with increase of Mach number supersonically.

Due to the rearward movement of the aerodynamic-centre position as the Mach number becomes supersonic (Fig. 15) it is the low-speed value which would govern the choice of c.g. position for an aircraft of this design to be stable. Although the wing is just neutrally stable about the present moment reference centre $0{\cdot}5\ \bar{c}$ at $M = 0{\cdot}3$ at $C_L = 0$, the C_L in level flight for an aircraft would be about $0{\cdot}45$, so that for neutral stability at 'take off' and 'landing' conditions the c.g. position should be located at 45% $\bar{c}$ or 3% c_0 forward of the present moment reference centre. Also with the present camber the wing will not trim in level flight with the c.g. at $0{\cdot}5\ \bar{c}$ at the cruise attitude ($M = 2{\cdot}2$, $C_L = 0{\cdot}075$), so that either additional camber or trailing-edge controls are necessary. Moving the c.g. position forward to $0{\cdot}45\ \bar{c}$ to give stability at $M = 0{\cdot}3$ greatly increases this trim problem at cruise conditions.

The drag polars (Figs. 16 and 17) have been analysed in terms of the minimum drag coefficient $C_{D\,m}$ and its corresponding value of lift coefficient $C_{L\,m}$. Plots of $(C_D - C_{D\,m})$ against $(C_L - C_{L\,m})^2$ are shown in Figs. 18 and 19. At supersonic speeds at high incidence $dC_D/dC_L{}^2$ is greater than at low incidence, whereas at subsonic speeds the reverse is true (Fig. 20). The graph of $K/\pi A/(dC_L/d\alpha)$, where $K = \pi A\ dC_D/d(C_L - C_{L\,m})^2$ and A is the wing aspect ratio, shows that this is due entirely to the large increase of $dC_L/d\alpha$ that occurs with increasing incidence at subsonic speeds. At incidence with no leading-edge suction $dC_D/d(C_L - C_{L\,m})^2$ is theoretically equal to $1/(dC_L/d\alpha)$.

The lift coefficient for minimum drag $C_{L\,m}$ and the minimum drag coefficient $C_{D\,m}$ corrected for shroud interference are shown in Fig. 21, together with the estimated skin-friction drag[5]. The net wave-drag coefficient varies from $0{\cdot}00385$ at $M = 1{\cdot}4$ to $0{\cdot}00265$ at $M = 2{\cdot}6$.

5.1.2. *Effect of fin and canopy.*—Adding both the fin and the canopy nose to the wing produces an increase in the minimum drag coefficient, the drag due to lift at both subsonic (Fig. 16) and supersonic speeds (Fig. 17) remaining unaltered. The minimum drag coefficient $C_{D\,m}$ is plotted in Fig. 22 and the increments in $C_{D\,m}$ due to the fin and canopy in Figs. 23 and 24 respectively. Comparison of estimated skin-friction drag[5] with measured fin drag (Fig. 23) suggests that the fin wave drag is small. (It's value in isolation would be about $0{\cdot}00022$ at $M = 1{\cdot}4$.) The reason for this is uncertain, since the fin does not appear to improve the cross-sectional area distribution significantly (Fig. 3). It is possible however, that at supersonic speeds, the fin pressure field could

induce positive pressures over the rear of the wing, thereby reducing the overall drag by interference. Although it would need pressure-distribution measurements to verify this idea, it is supported by the fact that the fin produces changes in lift and trim (Fig. 22). At subsonic speeds the fin produces a nose-down trim change with no effect on lift (Fig. 22). This again could possibly be due to pressures induced on the wing by the fin, the different sense of the trim change being due to the different fin pressure field at subsonic speeds.

The effect of the canopy is to produce a small loss of lift giving a nose-down pitching moment (Fig. 22) and more seriously a prohibitively large increase in wave drag. At $M = 2{\cdot}2$, this amounts to an increase of about 30% over the basic aircraft value (Figs. 21 and 24).

5.1.3. *Trailing-edge-control effectiveness.*—The effect of control setting ($-4°$ η_c inboard controls only, $-4°$ η_c inboard and outboard controls and $-4°$ ξ_c outboard controls only) on lift, pitching moment, rolling moment and drag is shown in Figs. 25 to 28. These graphs show that as might be expected there is no effect on lift-curve slope, aerodynamic-centre position or drag due to lift. The values of C_L, C_m and C_l at $\alpha = 0$ and $C_{D\,m}$ are replotted in Fig. 29. (There was no noticeable effect of the controls on $C_{L\,m}$.)

A comparison is made in Figs. 30 and 31 between the measured control effectiveness and theoretical values. The latter were obtained by three methods:

(i) Linear theory was used and full load carry-over onto the wing was assumed (lift induced by the control pressure field on that part of the wing lying within the Mach cone from the control leading-edge tip as in Ref. 6). The effect of the sting shroud on the inboard controls was allowed for in the manner of Ref. 7, that is the controls were treated as wings mounted on a body of diameter that of the sting shroud.

(ii) Using the results of pressure-distribution measurements on the symmetrical version of this wing reported in Ref. 2, the mean Mach number over the undeflected control was determined (slightly higher than the free-stream value because of the wing thickness). Using this Mach number a modified linear-theory estimate was obtained as in (i).

(iii) An allowance for wing thickness effects was made as in (ii) but all load carry-over was assumed zero. Each outboard control was assumed to act as an isolated rectangular wing. For the inboard controls the body was assumed to act as a reflection plate but to carry no load.

Figs. 30 and 31 show that the linear-theory estimate (with full load 'carry-over' onto the wing) is much too large at all Mach numbers. At high Mach numbers the same result is true of the two modified linear theories (with full load 'carry-over' onto the wing and with no load 'carry-over' onto the wing) although here the discrepancy is less. At low Mach number much better agreement is obtained, with the two modified linear estimates bracketing the measured values. In general these results are in agreement with those of Lord and Czarnecki[8, 9]. They found that although the control loadings due to incidence could be predicted with good accuracy using linear theory, the loadings due to control setting were much less than the theoretical values. This was mainly because the theory overestimated the pressure changes on the suction surface of the control (for control settings of the order of 10°). Away from the streamwise edges of the control a much closer prediction of the experimental pressures was obtained by Lord and Czarnecki using 'shock-expansion' theory over the controls. While the control settings used on the present model (4°) are lower than those used by Lord and Czarnecki in their tests, it is probable that part of the disparity between experiment and theory exists for similar reasons. This is borne out by the better agreement obtained with the

'modified linear' theory, which for small control settings is identical to the shock-expansion theory. Lord and Czarnecki also found that the lift carry-over at the ends of the control onto the wing, although not zero was much less than that predicted by theory. This effect, however, will be more noticeable at low Mach numbers where the theoretical lift carry-over is really significant. Although the gaps between the streamwise edges of the controls and wing are small at zero control deflection (0·3% of control chord) they become large as the control is deflected, allowing the suction surface of the wing to influence the pressure surface of the control or *vice-versa*. This is a possible reason why all three theoretical values of control effectiveness are higher than the measured values at the higher supersonic speeds.

Measured values of the parameter $(1/A_c)\, dC_{L\,c}/d\eta_c$ for both controls are plotted against $A_c \sqrt{(M^2-1)}$ in Fig. 32. (A_c is the control aspect ratio, $C_{L\,c}$ the lift coefficient based on control area and η_c the control deflection in radians). The aspect ratio of the inboard controls was taken as that of the two control panels joined together. As well as the values of $dC_{L\,c}/d\eta_c$ measured directly, other values were obtained from $dC_{m\,c}/d\eta_c$ and $dC_{l\,c}/d\xi_c$ by assuming that the centre of pressure of the control was at the centre of area. The differences between results in Fig. 32 for inboard and outboard controls are due to shroud interference. If the inboard control values are factored to allow for the carry-over lift on the sting shroud then the two sets of results collapse onto one line (Fig. 33). This interference factor obtained from Ref. 7 was based on the free-stream Mach number and varied from 1·217 at $M = 1{\cdot}4$ to 1·072 at $M = 2{\cdot}8$. Also shown in Fig. 33 is the linear-theory value for an isolated rectangular wing and the linear-theory two-dimensional value, factored by 0·7. This empirical expression for $(1/A_c)\, dC_{L\,c}/d\eta_c$ was suggested by Czarnecki and Lord in Ref. 10 and for $1 < A_c \sqrt{(M^2-1)} < 3$ it agrees very well with the present results, for $3 < A_c \sqrt{(M^2-1)} < 5$ it overestimates slightly.

5.1.4. *Effect of trailing-edge controls on drag.*—An expression for the increment in $C_{D\,m}$, (the minimum drag coefficient) due to control deflection is developed in Appendix I {equation (8)}:

$$\Delta C_{D\,m} = a_2'\,\eta_c^2 + \left(\frac{a_1' + a_2' + a_2''}{a_1}\right) \eta_c \left(C_{L\,m} - \Delta C_L\right) - \frac{\pi A}{K}\left[\eta_c \frac{(a_1' + a_2' + a_2'')}{2a_1}\right]^2$$

where

a_1 is $\left(\frac{dC_L}{d\alpha}\right)$ wing

a_1' is $\left(\frac{dC_L}{d\alpha}\right)$ control

a_2' is $\left(\frac{dC_L}{d\eta_c}\right)$ control

a_2'' is $\left(\frac{dC_L}{d\eta_c}\right)$ control carry-over lift

} based on wing area and per radian

η_c is control setting in radians (positive trailing edge down)

A is wing aspect ratio

K is drag due to lift factor

$C_{L\,m}$ is C_L at minimum drag

ΔC_L is lift on the wing at zero $\alpha_{T.E.}$ and η_c

$\alpha_{T.E.}$ is wing incidence (defined as the angle between the camber plane at the wing trailing edge and the free-stream direction).

For two controls (port and starboard) as elevators, the above increment is simply doubled, but for two controls as ailerons, we have:

$$\Delta C_{D\,m} = 2\left[a_2'\,\xi_c^2 - \frac{\pi A}{K}\left\{\xi_c \frac{(a_1' + a_2' + a_2'')}{2a_1}\right\}^2\right]$$

where ξ_c is the aileron setting in radians (positive trailing edge down on starboard wing, trailing edge up on port wing). Theoretical values of a_2' and a_2'' were obtained from:

(i) Linear theory with full lift carry-over.

(ii) Linear theory modified for wing thickness effects with full lift carry-over (cf. Section 5.1.3).

(iii) The empirical 'theory' of Ref. 10.

Using the above estimates together with measured values of a_1, K, $C_{L\,m}$, ΔC_L and a_1' (the last obtained from pressure-distribution measurements on the symmetrical model reported in Ref. 2), estimates of $C_{D\,m}$ have been obtained and are compared with measured values in Fig. 34. The agreement is fair considering the small size of the increments and the experimental accuracy.

Expressions are developed in Part 2 of Appendix I which enabled the drag of the trimmed wing $C_{D\,T}$ to be determined. Estimates of $C_{D\,T}$ obtained on the same basis as those of $C_{D\,m}$ are shown in Fig. 35 in comparison with measured values. Fair agreement is obtained between experiment and linear theory with full lift carry-over. Although the outboard controls produce more drag than the inboard controls for the same control setting, they also have a larger effect on the trimmed lift coefficient $C_{L\,T}$ (Fig. 36). Since a c.g. position at $0{\cdot}5\ \bar{c}$ would be unsatisfactory for flight at subsonic speeds, the curves of C_m against C_L have been redrawn for a moment reference centre of $0{\cdot}45\ \bar{c}$ (Fig. 37). Values of $C_{D\,T}$ have been evaluated at $C_L = 0{\cdot}075$ for both c.g. positions (using measured values of $C_{D\,T}$ at constant η_c and assuming that $C_{D\,T}$ varies linearly with $C_{L\,T}{}^2$) and these are plotted in Fig. 38 together with the untrimmed value of C_D at $C_L = 0{\cdot}075$. Moving the c.g. forward from $0{\cdot}50\ \bar{c}$ to $0{\cdot}45\ \bar{c}$ has a large adverse effect on the overall drag of the trimmed wing. In general the outboard controls are a slightly more efficient means of trimming the wing than the inboard controls.

5.2. *Lateral Stability.*

5.2.1. *Wing with basic nose and no fin at supersonic speeds.*—The variation of C_Y, C_n and C_l with β is slightly non-linear (Figs. 39, 40 and 41), with the non-linear side force acting ahead of the moment reference centre ($0{\cdot}692\ c_0$) and $dC_l/d\beta$ decreasing with β. A marked variation with incidence is displayed by the derivatives y_v and n_v (Figs. 42 and 43) and the incidence dependent y_v, together with its associated centre-of-pressure position, are shown in Figs. 44 and 45 respectively. Δy_v increases with incidence, gradually at first, but with a pronounced steepening of the curve at an incidence of 4° to 5°. Spence and Lean[4] have suggested that this sort of y_v variation with incidence is caused by the windward vortex approaching close to the wing surface under conditions of yaw, causing large suctions on the forward, sideward-facing upper surface. With this in mind, it might have been expected that the magnitude of the incidence dependent y_v would

decrease with Mach number, much in the same way as $(dC_L/d\alpha)_1 - (dC_L/d\alpha)_0$ (Fig. 15). In fact this does not happen. A small reduction only in Δy_v occurs with increasing Mach number. This would seem to indicate that the reduction in strength of the vortices at high Mach number is compensated for by the windward vortex approaching closer to the wing surface. Spence and Lean[4] give a value of $0{\cdot}49\ c_0$ as the low-speed value of the centre-of-pressure position $[(x_{\text{C.P.}})_y]$ of the incidence dependent y_v for an ogee wing ($s_T/C_0 = 0{\cdot}208$), and in Section 5.2.3 it is shown that at $M = 0{\cdot}3$ the experimental results agree fairly well with this value at high incidence. The rearward location of $(x_{\text{C.P.}})_y$ at supersonic speeds ($0{\cdot}6$ to $0{\cdot}7\ c_0$) and at low incidence at subsonic speeds, may be due to camber and the sting shroud, neither of which were present on the wing whose results were quoted by Spence and Lean.

Estimates of y_v and n_v at zero incidence have been made using slender-body theory. In order to reduce the labour involved, some simplifying assumptions have been made concerning the wing cross-section shape. Camber, both spanwise and chordwise, has been ignored. This omission is thought unlikely to have any significant effect on the derivatives. Estimates were made for two spanwise thickness distributions, a rhombic cross-section and a section consisting of a thin wing mounted symmetrically on a circular body. In both cases the maximum depth and span of the assumed section were identical with those of the wing at corresponding chordwise locations. Fig. 46 shows a comparison between actual and assumed spanwise thickness distributions at two chordwise locations. The conformal transformation for the rhombic cross-section is given in Ref. 11 and that for the wing body shape, together with the formulae for the derivatives in Ref. 12. Due to the complex variation of both wing thickness and span, numerical integration was used throughout to evaluate the derivatives. The measured values of $-(y_v)_{\alpha=0}$ show fair agreement with theory at $M = 1{\cdot}4$ but the disparity increases with Mach number until at $M = 2{\cdot}6$ the measured value is three times the theoretical value (Fig. 47). Since the cross-section shape falls somewhere between the extremes of wing-body and rhombic, it is probable that a realistic value of n_v can be obtained from the expression,

$$n_{v\,\text{true}} = \tfrac{1}{2}\,(n_{v\,\text{rhombic}} + n_{v\,\text{wing-body}}) + \Delta n_{v\,\text{due to sting fairing}}\,.$$

This gives an n_v of $-0{\cdot}0258$ which as in the case of y_v, agrees fairly well with the experimental results at $M = 1{\cdot}4$ but falls short at high Mach numbers. Poor agreement is obtained between theoretical and measured values of $(x_{\text{C.P.}})_y$.

In contrast to the above results $dl_v/d\alpha$ does not show any significant variation with α, however it does decrease with Mach number (Fig. 48). In Appendix II, using linear theory, an expression is developed for the body-axes rolling-moment derivative of thin cambered wings, based entirely on longitudinal loading using the lift-curve slope $dC_L/d\alpha$ and the longitudinal centre of pressure $x_{\text{C.P.}}/c_0$.

$$\frac{dl_{v\,B}}{d\alpha} = -\frac{dC_L}{d\alpha}\left(\frac{c_0}{b}\right)\left[1 - \frac{x_{\text{C.P.}}}{c_0}\right].$$

Although this is a theoretical expression it has been used with measured values of $dC_L/d\alpha$ and $x_{\text{C.P.}}/c_0$ (for the wing without fin at zero yaw) to give an estimate of $dl_{v\,B}/d\alpha$. The agreement between measured and predicted values of $dl_{v\,B}/d\alpha$ is only fair at $M = 1{\cdot}4$ (Fig. 49) and becomes progressively worse with increasing Mach number. This is probably due to the increasing importance of wing thickness effects as the flow normal to the wing leading edge approaches sonic

conditions. The importance of the Mach number normal to the leading edge is demonstrated in Fig. 50 where the quantity $l_{v\,B} - (l_{v\,B})_{\alpha=0}$ is plotted against α. For $M > 1{\cdot}7$, the values of $l_{v\,B} - (l_{v\,B})_{\alpha=0}$ collapse onto a single line when divided by $(1 - M^2 \cos^2 \Lambda_{\min})^{1/2}$. $\Lambda_{\min}$ is the minimum angle of sweepback of the wing. The slope of the collapsed curve is $0{\cdot}7$ times the slender-body thin-wing estimate for $dl_{v\,B}/d\alpha$. At Mach numbers less than $1{\cdot}7$ the results collapse onto a single curve for $\alpha < 6°$ whose slope is $0{\cdot}85$ times the slender-body thin-wing estimates. The design of this particular wing[1] is such that, theoretically, at the design lift coefficient ($C_L = 0$) the flow is attached along the entire wing leading edge. At incidences just above or below the design attitude it is expected that the flow will separate from the entire upper or lower surfaces respectively, so that separation from both upper and lower surface can never occur simultaneously. With sharp-edged plane delta wings at high Mach numbers where the leading edge becomes sonic (i.e. the theoretical design assumptions no longer hold), the leading-edge separation is suppressed and the flow becomes attached to the upper surface of the wing. Stanbrook and Squire[13] have analysed the results of tests on several sharp-edged plane delta wings in terms of the parameters, incidence normal to the leading edge, α_N and Mach number normal to the leading edge, M_N. Applied to the present wing this type of analysis shows that at incidence, attached flow could exist on the wing upper surface for Mach numbers above $1{\cdot}9$. It is suggested that the two curves of $l_{v\,B}$ (Fig. 50) represent two different types of flow at the wing leading edge. Below a Mach number of $1{\cdot}7$ the flow is separated along the entire leading edge with regions of attached flow existing above $M = 1{\cdot}7$. The difference between the predicted and measured Mach number boundary could possibly be due to camber. A similar result to the above was observed in tests on another slender wing of slightly different planform shape[14].

5.2.2. *Effect of canopy nose and fin at supersonic speeds.*—A feature of the results obtained with the fin present on the model (with and without canopy nose) is the presence of kinks in the curves of C_Y and C_n with β (Figs. 51, 52 and 53). These were also present at subsonic speeds (*see* Section 5.2.3) and are shown very clearly in Fig. 10. The transition from 'initial' to 'secondary' slope has been shown in the figures as a kink although it may in fact take up to $\frac{1}{2}$ degree of side-slip angle. The variation of C_l with β (Fig. 54) is slightly non-linear but does not contain any abrupt changes in slope.

The derivatives y_v, n_v and l_v are shown in Figs. 55, 56 and 57. The addition of the canopy nose to the wing with fin present has a negligible effect on y_v and l_v, but does result in a decrease in n_v. Although the n_v decrement is not very significant at low incidences only part of the large increase in n_v which occurs with increase of incidence with the basic nose is realized with the canopy nose. Since the wing was not tested with the canopy nose, without the fin (*see* Table 4), it is not possible to determine if the effect on n_v at high incidence is due simply to the presence of the canopy, or if it is caused by interference between canopy nose and fin. However, since there is little effect on y_v it is likely that there is some interference.

Any estimate of fin effectiveness must take into account interference between the fin and sting shroud. It is usual in cases of fin-body interference to use an interference factor based on slender-body theory[15]. With the present wing, for Mach numbers above $1{\cdot}4$, the fin is effectively isolated from the undersurface of the wing in so far as interference is concerned, so that the wing acts as an infinite reflection plane and symmetrical wing-body interference factors can be used to allow

for the sting shroud. Unpublished empirical interference factors* were used, and the lift-curve slope and aerodynamic-centre position of the fin were obtained from the charts of Ref. 16. The estimates of the side force and yawing-moment derivative contributions due to the fin, Δy_v and Δn_v respectively so obtained are given as theory I in Figs. 58 and 59. Measured values of fin effectiveness are in most cases less than theory I, and for both y_v and n_v they tend to decrease in size with incidence. An attempt has been made to produce a more accurate theoretical estimate including the effect of incidence on the derivatives. Using the results of pressure-distribution measurements on the symmetrical version of this wing[2], an estimate of the local Mach number in the region of the fin has been obtained at zero incidence, and its variation with incidence determined. Using values of fin lift-curve slope appropriate to this local Mach number, values of $\Delta y_{v\,\mathrm{fin}}$ and $\Delta n_{v\,\mathrm{fin}}$ were obtained (theory II in Figs. 58 and 59). In most cases this estimate of fin effectiveness is in good agreement with the measured values and accurately predicts the variation of $\Delta y_{v\,\mathrm{fin}}$ and $\Delta n_{v\,\mathrm{fin}}$ with incidence. This would seem to indicate a lack of wing vortex interference on the fin at small angles of yaw for $\alpha < 12°$. The simple theory overestimates $\Delta l_{v\,B\,\mathrm{fin}}$ at all Mach numbers (Fig. 60) and at $M = 1{\cdot}4$ the measured value is positive whereas the theoretical value is negative. Since $\Delta y_{v\,\mathrm{fin}}$ does not show any abnormalities at $M = 1{\cdot}4$, the reversed direction of $\Delta l_{v\,B\,\mathrm{fin}}$ cannot be caused by sidewash fields acting on the fin, leaving as the only possibility, interference on the wing by the fin pressure field.

The increase in y_v at values of sideslip above about 2° (Fig. 51) is plotted in Fig. 61 as Δy_v (secondary y_v – initial y_v) together with its associated centre-of-pressure position for the configuration with basic nose and fin (Fig. 62). In general the centre-of-pressure position is located in the region of the fin and it is reasonable to assume that the kink is due to an increase in fin lift-curve slope resulting from fin leading-edge flow-separation effects. It would be expected that the additional y_v would decrease as the fin leading edge approached sonic conditions and flow separation was suppressed. That this does in fact happen is shown in Fig. 63 where ΔC_Y due to the fin is plotted against β for several Mach numbers†. The increase in slope of the curve of C_Y plotted against β for the configuration with fin is due entirely to fin effects at $M = 1{\cdot}4$ whereas at $M = 2{\cdot}6$ it is due entirely to wing flow effects.

5.2.3. *Subsonic results, wing with basic nose and fin.*—Variation of the coefficients C_Y, C_n and C_l with β is shown in Figs. 64, 65 and 66. As at supersonic speeds there are kinks in the C_Y and C_n curves. The derivatives y_v, n_v and l_v (Fig. 67) are little different at $M = 0{\cdot}3$ and $0{\cdot}8$ for $R = 2 \times 10^6$ per foot, and at $M = 0{\cdot}3$, Reynolds number has a negligible effect.

---

* If d is the body diameter, and s_F is the fin semi-span measured from the body centre-line, then the empirical interference factors (ratio of sideforce on a body mounted fin to that on a reflection plane mounted fin) for a configuration with no afterbody, can be approximated by

$$1 + 0{\cdot}688\,\frac{d}{s_F},$$

compared with the slender-body theory value of

$$\left(1 + 0{\cdot}50\,\frac{d}{s_F}\right)^2.$$

Both of the expressions are independent of fin taper ratio.

† It should be noted that because of lack of data with fin on at $M = 2{\cdot}6$ the values were interpolated from those at $M = 2{\cdot}4$ and $2{\cdot}8$. Data with fin off is not available at $M = 2{\cdot}8$.

The incidence dependent y_v and its associated centre-of-pressure position have been obtained and are plotted in Figs. 68 and 69 respectively. There is a decrease in Δy_v between $M = 0{\cdot}3$ and $0{\cdot}8$ and again between $M = 0{\cdot}8$ and $1{\cdot}4$. A pronounced steepening of the curve of Δy_v occurs between $\alpha = 12°$ and $\alpha = 16°$. No measurements of lateral loads at subsonic speeds were made without the fin. However the absence of any wing vortex interference with the fin at supersonic speeds was demonstrated in Section 5.2.2. The assumption that this result also holds at subsonic speeds enables a comparison to be made between the present results and those of Spence and Lean[4]. Good agreement is obtained between the centre-of-pressure position of the incidence dependent y_v at high incidence and the low speed value of $0{\cdot}49\ c_0$ from Ref. 4. At low incidence $(x_{\text{C.P.}})_y$ is much further aft and approaches the supersonic value of $0{\cdot}7\ c_0$ at $\alpha = 4°$.

The increment in y_v (defined as Δy_v = secondary y_v − initial y_v), does not vary significantly with incidence for $\alpha < 16°$, whereas, above this incidence it behaves rather erratically (Fig. 70). A similar variation is shown by the centre-of-pressure position of this incremental y_v. It remains in the region of the fin up to an incidence of 16° (Fig. 71) and then moves forward to $0{\cdot}31\ c_0$ at $\alpha = 20{\cdot}4°$.

Estimates of y_v and n_v at subsonic speeds have been made using the same methods as were employed at supersonic speeds, with the exception that the fin sting-shroud interference factor was obtained from Ref. 15. Fair agreement between theory and experiment is obtained at low incidence, but it gets progressively worse as the incidence increases (Fig. 72).

In the previous section (5.2.2) it was shown that at $M = 1{\cdot}4$ the measured fin effectiveness on l_v was of opposite sign to theory. The results of tests on another slender-wing model fitted with the same fin[14] have demonstrated this same effect and shown that it also occurs at subsonic speeds. It is not unreasonable therefore to assume that this effect extends down to $M = 0{\cdot}3$ with the present wing. For this reason no attempt has been made to include the effect of the fin on the theoretical prediction of the body-axes rolling-moment derivative $l_{v\,B}$. Slender-body estimates of $l_{v\,B}$ using four different cross-section shapes have been obtained in addition to an estimate based on the method of Appendix II and using measured values of C_L and $(x_{\text{C.P.}})$. Cross-section shape has only a small effect on the theoretical value of $dl_{v\,B}/d\alpha$ and all estimates show good agreement with measured $dl_{v\,B}/d\alpha$ at small incidence. The effectiveness of this fin on $l_{v\,B}$ at $M = 0{\cdot}3$ as measured in Ref. 14 was $0{\cdot}007$ and if allowance is made for this increment, then $l_{v\,B}$ can be predicted with fair accuracy up to incidences of about 10°. The expression:

$$l_{v\,B} = -\left\{ C_L\left(\frac{c_0}{b}\right)\left[1 - \frac{x_{\text{C.P.}}}{c_0}\right]\right\}_{\text{Experimental}}$$

although predicting the trend of $l_{v\,B}$ with incidence overestimates its magnitude at all incidences. This expression for $l_{v\,B}$ applies strictly to wings of zero thickness only. It is possible, therefore, that the disparity between experimental values of $l_{v\,B}$ and those predicted using the above expression result from wing thickness effects.

6. *Conclusions.*

Longitudinal Stability.

(a) Within the M range tested the most forward position of the aerodynamic centre occurs at low speeds, and hence the low-speed value would dictate the centre-of-gravity position of an actual aircraft design, which would be at $0{\cdot}45\ \bar{c}$ for neutral stability at $C_L = 0{\cdot}45$. The most aft aerodynamic-centre position occurs at $M = 1{\cdot}4$ and at Mach numbers above $1{\cdot}4$ it moves forward again.

(b) For the configuration with basic nose and no fin the centre of pressure at the cruise attitude ($M = 2{\cdot}2$, $C_L = 0{\cdot}075$) is at $53{\cdot}3\%\ \bar{c}$ and hence the wing would be untrimmed by $8{\cdot}3\%\ \bar{c}$.

(c) The canopy shape tested is unsatisfactory, because of its large wave-drag increment (31% of the wave drag of the wing with the basic nose).

(d) The fin produces a negligible wave-drag increment possibly due to interference between the fin pressure field and the rear upper surface of the wing.

(e) Trailing-edge control effectiveness is less than that predicted by linear theory but agrees quite well with the estimates based on the empirical method of Ref. 10. The drag increments due to the controls for both the untrimmed and the trimmed wing show fair agreement with theory. In general the outboard controls are slightly more efficient than the inboard controls as a means of trimming the wing.

Lateral Stability.

(a) With the basic nose and no fin, there is a marked variation of y_v with α, the centre of pressure of the incidence dependent y_v varying from $0{\cdot}7\ c_0$ at low incidence to $0{\cdot}5\ c_0$ at high incidence ($\alpha = 20°$, $M = 0{\cdot}3$).

(b) The measured values of y_v and $n_{v\,B}$ at zero incidence show fair agreement with slender-body theory at $M = 1{\cdot}4$ but the theory underestimates at higher Mach numbers. Although $l_{v\,B}$ can be predicted with fair accuracy at subsonic speeds using slender-body theory, the agreement at supersonic speeds with linear theory is poor. $dl_{v\,B}/d\alpha$ varies significantly with Mach number at supersonic speeds but a correlation is possible on the basis of the Mach number normal to the wing leading edge.

(c) The canopy nose, in conjunction with the fin at supersonic speeds, causes a reduction in n_v which although small at low incidence is quite significant at high incidence. It has no effect on either y_v or l_v.

(d) In general the effect of the fin on y_v and n_v at supersonic speeds can be predicted with good accuracy, when the side force on the fin is based on the local Mach number in the region of the fin rather than the free-stream value.

SYMBOLS

A Aspect ratio

$a_1 = \left(\frac{dC_L}{d\alpha}\right)$ wing

$a_1' = \left(\frac{dC_L}{d\alpha}\right)$ control, based on wing area

$a_2' = \left(\frac{dC_L}{d\eta_c}\right)$ control, based on wing area

$a_2'' = \left(\frac{dC_L}{d\eta_c}\right)$ control carry-over lift, based on wing area

b Wing span

c Wing chord

c_0 Wing root chord

$\bar{c}$ Aerodynamic mean chord

C_p Pressure coefficient, $(p-p_\infty)/q$

C_L Lift coefficient, lift/qS (positive upwards)

C_m Pitching-moment coefficient, pitching moment/$qS\bar{c}$ (positive nose up)

C_D Drag coefficient, drag/qS (positive downstream)

C_Y Side force coefficient, side force/qS (positive to starboard)

C_X Axial force coefficient, force along balance axis/qS (positive backwards)

C_n Yawing-moment coefficient, yawing moment/qSb (positive nose to starboard)

C_l Rolling-moment coefficient, rolling moment/qSb (positive starboard wing downwards)

d Body diameter

$h = \frac{dC_m}{dC_L}$

K Drag-due-to-lift factor, $\frac{\partial C_D}{\partial (C_L - C_{L\,m})^2} \times \pi A$

$l_{(x,\,y)}$ Local wing loading $= -\Delta C_p = -(C_{pu} - C_{p\,L})$

$l_v = \left(\frac{\partial C_l}{\partial \beta}\right)$ per radian

M Mach number

$n_v = \left(\frac{\partial C_n}{\partial \beta}\right)$ per radian

p Local static pressure

SYMBOLS—*continued*

τ	Wing volume/(wing area)$^{3/2}$
φ	Perturbation velocity potential, $\varphi = \varphi_0 + \alpha\varphi_1 + \beta\varphi_2$
Φ	Roll angle measured from trailing edge horizontal (positive starboard wing tip down)
θ	Total incidence (positive nose up)

Suffices

B	Refers to body axes
c	Refers to control
L	Refers to lower surface of wing
m	Refers to conditions at minimum drag
N	Refers to conditions normal to wing leading edge
0	Refers to conditions at zero lift
T	Refers to trimmed conditions
T.E.	Refers to conditions at wing trailing edge
u	Refers to upper surface of wing
y	Refers to yaw plane
1	Refers to increased value of $\mathrm{d}C_L/d\alpha$ and K at high incidence

REFERENCES

No.	Author(s)	Title, etc.
1	J. Weber	Design of warped slender wings with the attachment line along the leading edge. R.A.E. Tech. Note No. Aero. 2530. A.R.C. 20 051. September, 1957.
2	C. R. Taylor	Measurements at Mach numbers up to 2·8 of the longitudinal characteristics of one plane and three cambered slender 'ogee' wings. A.R.C. R. & M. 3328. December, 1961.
3	S. B. Berndt	Wind tunnel interference due to lift for delta wings of small aspect ratio. K.T.H. Aero. Tech. Note 19. Sweden. 1952.
4	A. Spence and D. Lean	Some low speed problems of high speed aircraft. *J. R. Ae. Soc.*, Vol. 66, No. 616, p. 217. April, 1962.
5	— .	Royal Aeronautical Society Data Sheets, Aerodynamics, Vol. 2.
6	P. A. Lagerstrom and M. E. Graham	Linearised theory of supersonic control surfaces. *J. Ae. Sci.*, Vol. 21, pp. 31 to 34. January, 1949.
7	W. C. Pitts, J. N. Nielson and G. E. Kaattari.	Lift and center of pressure of wing-body-tail combinations at subsonic, transonic and supersonic speeds. N.A.C.A. Report 1307. 1957.
8	D. R. Lord and K. R. Czarnecki ..	Pressure distribution and aerodynamic loadings for several flap-type trailing-edge controls on a trapezoidal wing at Mach numbers 1·61 and 2·01. N.A.C.A. Research Memo. L55J03 (TIL/5013). March, 1956.
9	K. R. Czarnecki and D. R. Lord ..	Load distribution associated with controls at supersonic speeds. N.A.C.A. Research Memo. L53D15a (TIB/3746). May, 1953.
10	K. R. Czarnecki and D. R. Lord ..	Simplified procedures for estimating flap-control loads at supersonic speeds. N.A.C.A. Research Memo. L55E12 (TIB/4692). May, 1955.
11	A. J. Ross	The calculation of lateral stability derivatives of slender wings at incidence, including fin effectiveness, and correlation with experiment. A.R.C. R. & M. 3402. March, 1961.
12	A. H. Sacks	Aerodynamic forces, moments and stability derivatives for slender bodies of general cross section. N.A.C.A. Tech. Note. 3283. November, 1954.
13	A. Stanbrook and L. C. Squire ..	Possible types of flow at swept leading edges. *Aero. Quart.* Vol. XV, Part 1, pp. 72 to 82. February, 1964.
14	D. Isaacs	Lateral stability measurements including the effect of a fin on a slender cambered wing at subsonic and supersonic speeds. R.A.E. in preparation.
15	F. K. Goodwin and G. E. Kaattari ..	Estimation of directional stability derivatives at small angles and subsonic and supersonic speeds. N.A.S.A. Memo. 12–2–58A (TIL/6338). December, 1958.
16	A. Stanbrook	The lift-curve slope and aerodynamic centre position of wings at subsonic and supersonic speeds. A.R.C. 17 615. November, 1954.

APPENDIX I

The Effect of Trailing-Edge Controls on the Drag of a Cambered Wing

Part 1. *Minimum Drag Coefficient.*

It is assumed that the camber surface is planar over the region of the trailing-edge controls. With the controls undeflected, assume that the lift and drag coefficient of the wing can be expressed as

$$C_L = a_1\alpha_{\text{T.E.}} + \Delta C_L \tag{1}$$

$$C_D = C_{D\,m} + \frac{K}{\pi A}(C_L - C_{L\,m})^2 \tag{2}$$

when C_L and C_D are the lift and drag coefficients respectively.

$\alpha_{\text{T.E.}}$ is the wing incidence (the angle between the camber plane at the trailing edge and the free-stream direction).

K is the drag due to lift factor

A is the wing aspect ratio

a_1 is the lift-curve slope of the wing with respect to $\alpha_{\text{T.E.}}$

ΔC_L is the lift on the wing at zero $\alpha_{\text{T.E.}}$ and η_c

Suffix m refers to conditions at minimum drag.

If the control is now deflected and $\alpha_{\text{T.E.}}$ is kept constant, then for both $\alpha_{\text{T.E.}}$ and η_c small, the modified coefficients are

$$C_L' = C_L + (a_2' + a_2'')\eta_c \tag{3}$$

$$C_D' = C_D + a_2'\eta_c(\alpha_{\text{T.E.}} + \eta_c) + a_2''\alpha_{\text{T.E.}}\eta_c + (a_1'\alpha_{\text{T.E.}} + \Delta C_{L\,c})\eta_c \tag{4}$$

where η_c is the control deflection (positive trailing edge downwards)

a_2' is the lift-curve slope of the control with respect to η_c

a_2'' is the lift-curve slope of the control 'carry-over' lift with respect to η_c

a_1' is the lift-curve slope of the control with respect to $\alpha_{\text{T.E.}}$

$\Delta C_{L\,c}$ is the lift on the control at zero $\alpha_{\text{T.E.}}$ and η_c.

Using equations (1), (2) and (3) to eliminate C_D and $\alpha_{\text{T.E.}}$ from equation (4) and assuming $\Delta C_{L\,c}$ is small enough to be ignored we get

$$C_D' = C_{D\,m} + \frac{K}{\pi A}[C_L' - \eta_c(a_2' + a_2'') - C_{L\,m}]^2 + a_2'\eta_c^2 + \\ + \left(\frac{a_1' + a_2' + a_2''}{a_1}\right)\eta_c\,[C_L' - \Delta C_L - \eta_c(a_2' + a_2'')]. \tag{5}$$

This equation can be re-arranged to give

$$C_D' = C_{D\,m}' + \frac{K}{\pi A}(C_L' - C_{L\,m}')^2 \tag{6}$$

where $C_{D\,m}'$ and $C_{L\,m}'$ are the new values of $C_{D\,m}$ and $C_{L\,m}$ and are given by

$$C_{L\,m}' - C_{L\,m} = (a_2' + a_2'')\eta_c - \frac{\pi A}{K}\left[\frac{\eta_c(a_1' + a_2' + a_2'')}{2a_1}\right]. \tag{7}$$

$$C_{D\,m}' - C_{D\,m} = a_2'\eta_c^2 + \left(\frac{a_1' + a_2' + a_2''}{a_1}\right)\eta_c(C_{L\,m} - \Delta C_L) - \frac{\pi A}{K}\left[\frac{\eta_c(a_1' + a_2' + a_2'')}{2a_1}\right]^2. \tag{8}$$

For an uncambered wing with no control lift 'carry-over' these two equations reduce to

$$C_{L\,m}' - C_{L\,m} = a_2'\eta_c - \frac{\pi A}{K}\left[\frac{\eta_c(a_1' + a_2')}{2a_1}\right] \tag{9}$$

$$C_{D\,m}' - C_{D\,m} = a_2'\eta_c^2 - \frac{\pi A}{K}\left[\frac{\eta_c(a_1' + a_2')}{2a_1}\right]^2. \tag{10}$$

Part 2. Drag of the Trimmed Wing.

With controls undeflected the pitching moment of the wing can be expressed as

$$C_m = C_{m\,0} + hC_L \tag{11}$$

where h is the value of dC_m/dC_L.

If the control is now deflected

$$C_m' = C_{m\,0} + hC_L - (a_2' + a_2'')\eta_c\bar{x}_c \tag{12}$$

where $\bar{x}_c = x_c/\bar{c}$ and x_c is the distance from the moment reference centre to the control centre of pressure (positive backwards). Using equation (3) to eliminate C_L from (12) we have

$$C_m' = C_{m\,0} + hC_L' - (a_2' + a_2'')\eta_c(h + \bar{x}_c) \tag{13}$$

and for trimmed flight $C_m' = 0$, so that we arrive at an expression relating the trimmed lift coefficient $C_{L\,T}'$ and the control angle to trim $\eta_{c\,T}$:

$$C_{L\,T}' = \frac{\eta_{c\,T}(a_2' + a_2'')(h + x_c) - C_{m\,0}}{h} \tag{14}$$

It is convenient in comparing this method of estimation with experiments to determine $C_{L\,T}'$ for the control setting $\eta_{c\,T}$ actually tested rather than to determine a control setting for a given trimmed lift coefficient by interpolation. Equation (14) enables $C_{L\,T}'$ to be estimated using measured values of $\eta_{c\,T}$, h and $C_{m\,0}$ and theoretical values of a_2', a_2'' and $\bar{x}_c$. In order to determine the drag of the trimmed wing it is necessary to know $C_{L\,m}'$ and $C_{D\,m}'$. These are given by equations (7) and (8) respectively, writing $\eta_{c\,T}$ for η_c. As in the expression for $C_{L\,T}'$, theoretical values of a_2' and a_2'' are used in (7) and (8) together with measured values of all the other parameters (obtained from the basic wing results with zero control deflection). The drag of the trimmed wing is then given by (6), writing $C_{D\,T}'$ and $C_{L\,T}'$ for C_D' and C_L' respectively.

APPENDIX II

The Body-Axes Rolling Moment of a Thin Cambered Wing

For cambered wings with zero thickness it is possible to derive a simple relationship between the body-axes rolling-moment derivative $\partial l_{v\,B}/\partial\alpha$, the lift coefficient C_L and the chordwise location of the pitch plane centre of pressure $x_{\text{C.P.}}$.

With the usual assumptions of linearized theory the perturbation velocity potential for the flow past an infinitely thin cambered wing at incidence α and sideslip β can be written:

$$\varphi = \varphi_0 + \alpha\varphi_1 + \beta\varphi_2 + \mathrm{O}(\alpha^2, \beta^2) \tag{15}$$

where φ_0 is the potential at $\alpha = 0$

$\alpha\varphi_1$ is the potential due to incidence α at $\beta = 0$

$\beta\varphi_2$ is the potential due to the additional local incidence $+ \beta\partial z/\partial y$,

and $z = z_c(x, y)$ is the equation for the camber surface.

The loading on the wing is given by

$$\begin{aligned} l_{(x,y)} &\equiv -(C_{p\,u} - C_{p\,L}) \\ &= +\frac{4}{U}(\varphi_x - \beta\varphi_y) + \mathrm{O}(\alpha^2, \beta^2), \end{aligned} \tag{16}$$

the velocity potential being evaluated on the upper surface of the wing. Here U is the free-stream velocity and x, y, z are right-handed Cartesian body co-ordinates with origin O at the wing leading-edge apex and axes Ox, Oy, and Oz pointing downstream, to starboard and vertically upwards respectively at $\alpha = \beta = 0$ (the suffices x and y refer to partial differentials of φ with respect to these quantities).

The body-axes rolling-moment coefficient is

$$C_{l\,B} = -\frac{4}{USb}\iint_S (\varphi_x - \beta\varphi_y) y\, dx\, dy + \mathrm{O}\left(\alpha^2, \beta^2, z_c\frac{\partial z_c}{\partial y}\right) \tag{17}$$

where S is the wing plan area and b the wing span.

Since for a wing with symmetrical camber {i.e. $z_c(x, y) = z_c(x, -y)$}, φ_0 and φ_1 are even functions of y and φ_2 is an odd function of y, the above equation for $C_{l\,B}$ can be rewritten as

$$\begin{aligned} C_{l\,B} &= \frac{4\beta}{USb}\iint_S (\varphi_{0\,y} + \alpha\varphi_{1\,y} - \varphi_{2\,x}) y\, dx\, dy + \mathrm{O}\left(\alpha^2, \beta^2, z_c\frac{\partial z_c}{\partial y}\right) \\ &= -\frac{4\beta}{USb}\iint_S (\varphi_0 + \alpha\varphi_1) dx\, dy - \frac{4\beta}{USb}\int_{-b/2}^{+b/2} [\varphi_2]_{\text{T.E.}}\, y\, dy \end{aligned} \tag{18}$$

since $\varphi_0 = \varphi_1 = \varphi_2 = 0$ at the wing leading edges.

The corresponding lift and pitching-moment coefficients at zero yaw are:

$$\begin{aligned} C_L &= \frac{4}{US}\iint_S (\varphi_{0\,x} + \alpha\varphi_{1\,x})\, dx\, dy \\ &= \frac{4}{US}\int_{-b/2}^{+b/2} [\varphi_0 + \alpha\varphi_1]_{\text{T.E.}}\, dy \end{aligned} \tag{19}$$

and

$$C_m = -\frac{4}{USc_0}\iint_S (\varphi_{0\,x} + \alpha\varphi_{1\,x})\, x\, dx\, dy$$

where c_0 is the root chord

$$C_m = -\frac{4}{US}\int_{-b/2}^{+b/2}[\varphi_0 + \alpha\varphi_1]_{\text{T.E.}}\,dy + \frac{4}{USc_0}\iint_S(\varphi_0+\alpha\varphi_1)\,dx\,dy\,. \tag{20}$$

Combining (18), (19) and (20) gives

$$C_{l\,B} = -\beta\frac{c_0}{b}(C_m+C_L) - \frac{4\beta}{USb}\int_{-b/2}^{+b/2}[\varphi_2]_{\text{T.E.}}y\,dy \tag{21}$$

or

$$l_{v\,B} = -\frac{c_0}{b}C_L\left\{1-\frac{x_{\text{C.P.}}}{c_0}\right\} - \frac{4}{USb}\int_{-b/2}^{+b/2}[\varphi_2]_{\text{T.E.}}y\,dy \tag{22}$$

The latter term represents the contribution of spanwise droop or dihedral to $l_{v\,B}$. At speeds where the wing is aerodynamically slender, linear theory degenerates into slender-wing theory, and here the effects on $l_{v\,B}$ of camber depend only on the spanwise camber at the wing trailing edge. For the present wing the spanwise camber is negligible at the trailing edge and equation (22) reduces to

$$l_{v\,B} = -\frac{c_0}{b}C_L\left\{1-\frac{x_{\text{C.P.}}}{c_0}\right\}\ (M\leqslant 1{\cdot}0) \tag{23}$$

At supersonic speeds $[\varphi_2]_{\text{T.E.}}$ can be obtained by a surface integral but since it is independent of α there does exist the simple relationship

$$\frac{dl_{v\,B}}{d\alpha} = -\frac{c_0}{b}\frac{dC_L}{d\alpha}\left\{1-\frac{x_{\text{C.P.}}}{c_0}\right\} \tag{24}$$

TABLE 1

Principal Dimensions of the Model

Wing

Equation of leading edge $y = s(x)$

$$s(x) = s_T \left(\frac{x}{c_0}\right) \left[1{\cdot}2 - 2{\cdot}4 \left(\frac{x}{c_0}\right) + 2{\cdot}2 \left(\frac{x}{c_0}\right)^2 + 3 \left(\frac{x}{c_0}\right)^3 - 3 \left(\frac{x}{c_0}\right)^4\right].$$

Equation of spanwise camber shoulder line $y = s(x)\eta_0(x)$

$$\eta_0(x) = 0{\cdot}5 \qquad \left(\frac{x}{c_0}\right) \leqslant 0{\cdot}5$$

$$\eta_0(x) = 0{\cdot}5 + \left(\frac{x}{c_0} - 0{\cdot}5\right)^2 \qquad \left(\frac{x}{c_0}\right) > 0{\cdot}5$$

Gross area	4·680 sq. ft
Span	2·08 ft
Root chord	5·00 ft
Semi-span to root chord ratio (s_T/c_0)	0·2081
Aerodynamic mean chord	3·079 ft
Aspect ratio	0·924
Moment-reference-centre position (measured from trailing edge) $\bar{c}/2$	1·539 ft
Ratio of wing area to area of enclosing rectangle (P)	0·450
Wing volume (v)	725·4 cu. in.
Non-dimensionalized wing volume τ = wing volume/(area)$^{3/2}$	0·0415

Fin

Area	0·314 sq. ft
Height	4·762 in.
Root chord	15·832 in.

TABLE 2

Basic Fin Section (Root Chord)

Distance from leading edge (inches)	Semi-thickness (inches)
0	0·0050
0·7916	0·0509
1·5832	0·0905
2·3748	0·1269
3·1663	0·1570
3·9579	0·1839
4·7495	0·2045
5·5411	0·2219
6·3327	0·2330
7·1243	0·2409
7·9159	0·2425
8·7074	0·2409
9·4990	0·2330
10·2906	0·2219
11·0822	0·2045
11·8738	0·1839
12·6654	0·1570
13·4569	0·1269
14·2485	0·0905
15·0401	0·0509
15·8317	0·0050

TABLE 3

Control Setting Angles (Controls Unloaded)

Location of control	Nominal setting (degrees)	True setting (degrees)
Port outboard	−4 +4	−3·96 +4·03
Port inboard	−4	−3·68
Starboard outboard	−4	−4·04
Starboard inboard	−4	−3·98

TABLE 4

Test Programme

Nose shape	Fin	Inboard controls (deg)	Outboard controls (deg)	Reynolds No. per foot	Mach No. range	Remarks
Basic	OFF	0	0	2×10^6	0·3, 0·8	C_L, C_m and C_D measured only
Basic	OFF	0	0	2×10^6	1·4, 1·6, 1·8, 2·0, 2·2, 2·4, 2·6, 2·8	
Basic	ON	0	0	2×10^6	0·3, 0·8, 1·4, 1·8, 2·2, 2·4, 2·8	
Basic	ON	0	0	8×10^6	0·3	
Canopy	ON	0	0	2×10^6	1·4, 1·8, 2·2, 2·4, 2·8	
Basic	ON	−4	0	2×20^6	1·4, 1·8, 2·2, 2·4, 2·8	
Basic	ON	−4	−4	2×10^6	1·4, 1·8, 2·2, 2·4, 2·8	
Basic	ON	0	±4	2×10^6	1·4, 1·8, 2·2	

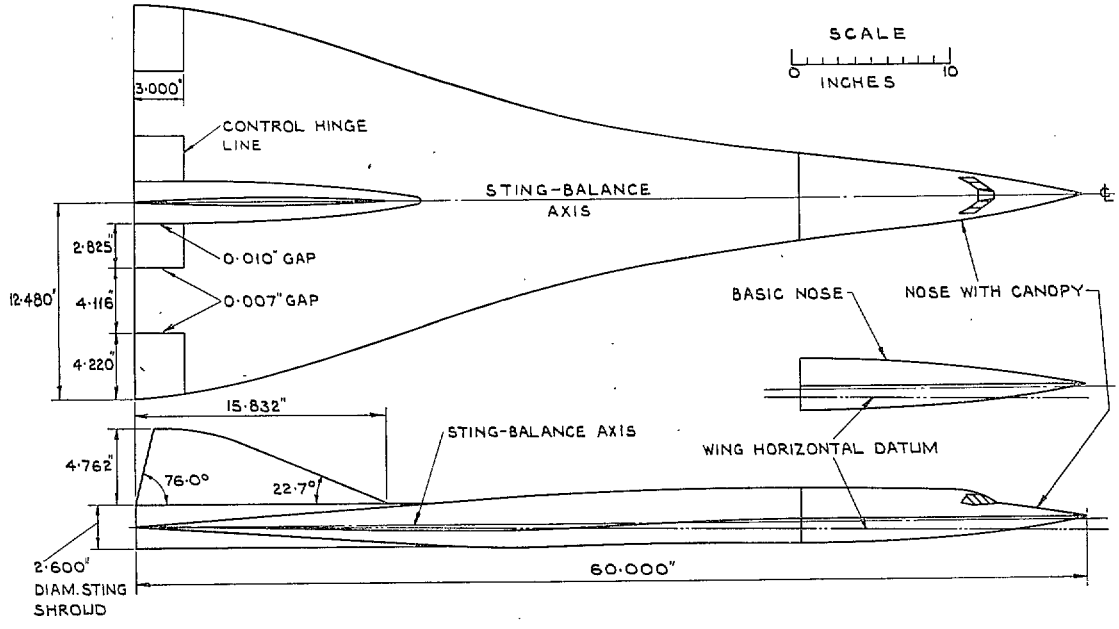

FIG. 1. General arrangement of the model.

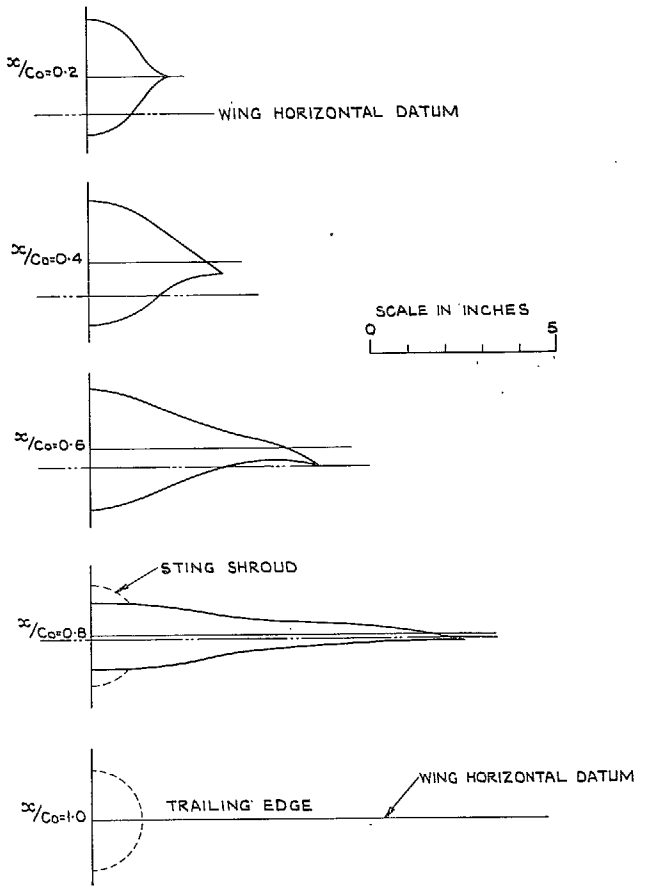

FIG. 2. Details of wing cross-section.

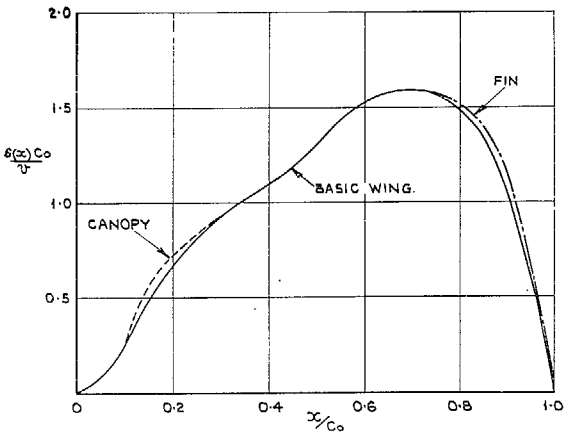

FIG. 3. Cross-section area distribution.

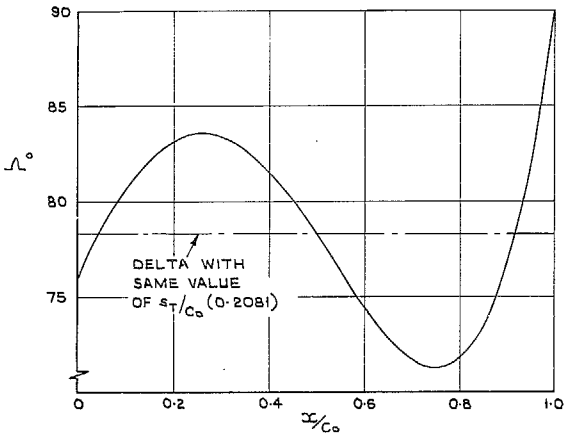

FIG. 4. Variation of leading-edge sweepback angle along the wing.

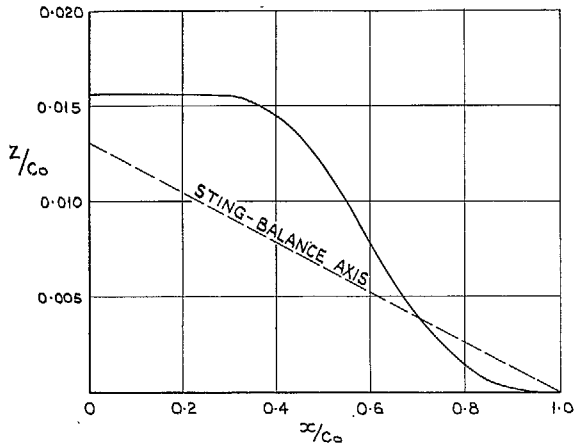

FIG. 5. Camber shape on wing centre line relative to wing horizontal datum.

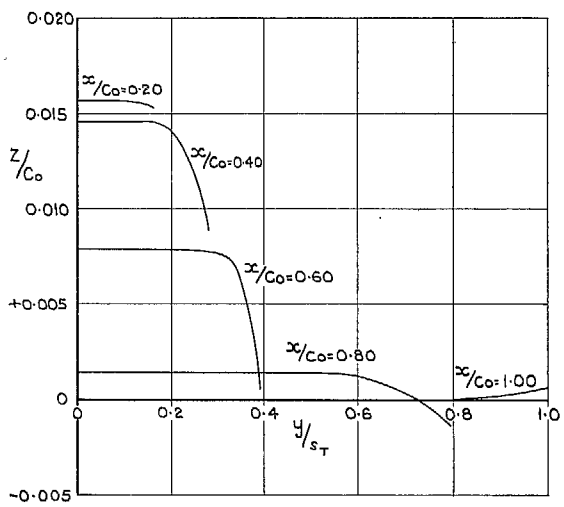

FIG. 6. Spanwise camber shapes relative to wing horizontal datum.

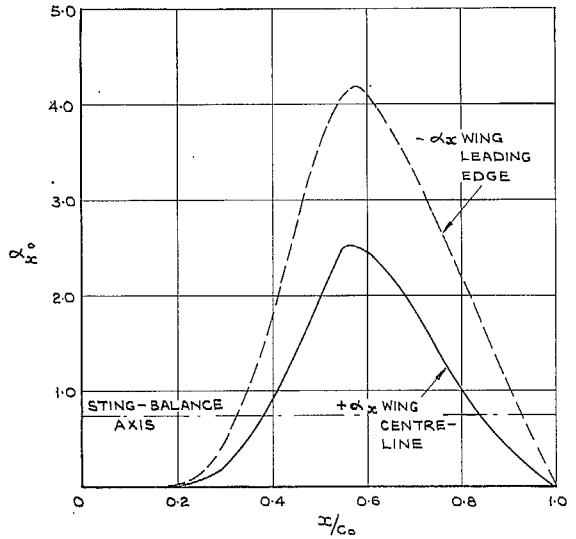

FIG. 7. Wing local incidence distribution relative to wing horizontal datum.

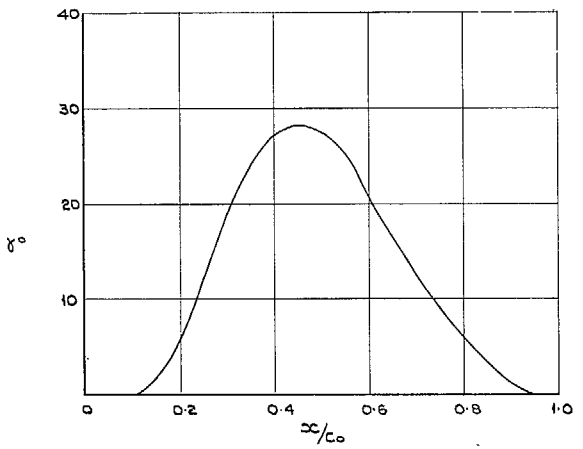

FIG. 8. Wing leading-edge spanwise droop relative to wing horizontal datum.

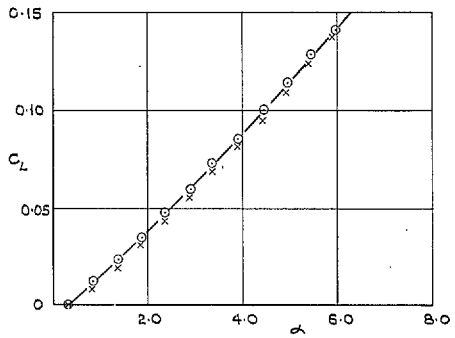

VARIATION OF C_L WITH α

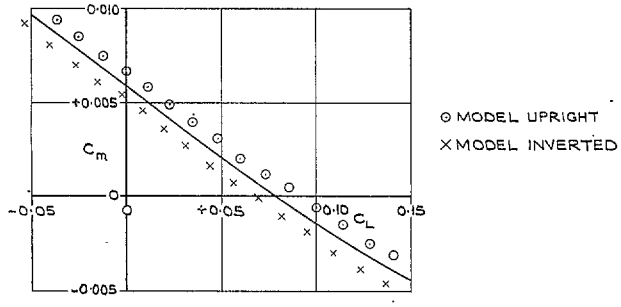

VARIATION OF C_m WITH C_L

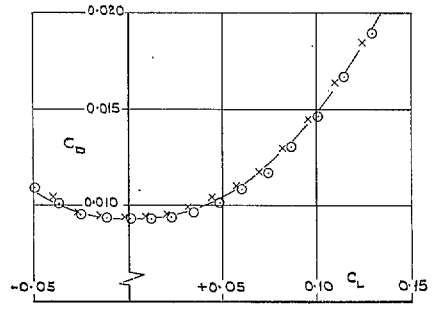

VARIATION OF C_D WITH C_L

FIG. 9. Typical results showing derivation of mean curve; wing with fin, basic nose and inboard controls ($\eta_c = -4°$), $M = 1{\cdot}8$.

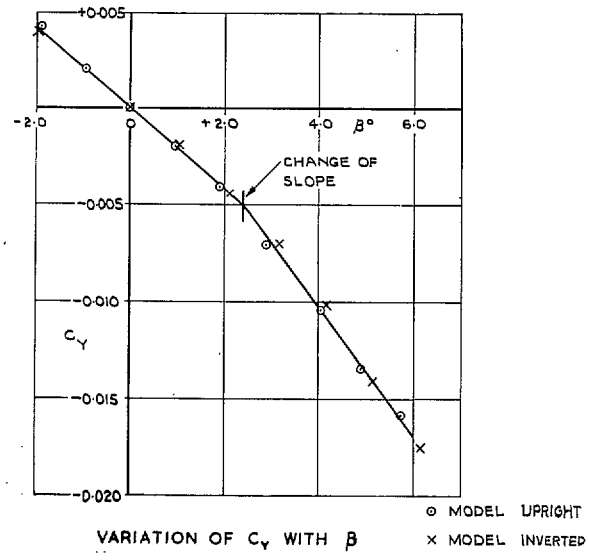

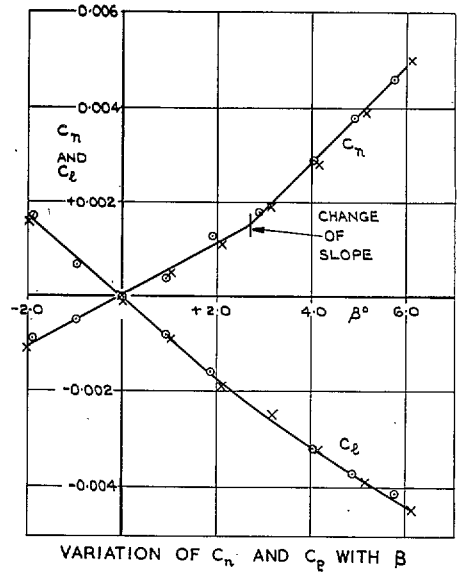

FIG. 10. Typical results showing derivation of mean curve; wing with fin and basic nose, $M = 0{\cdot}3$, $R = 8 \times 10^6$ per ft, $\alpha = 4{\cdot}22°$.

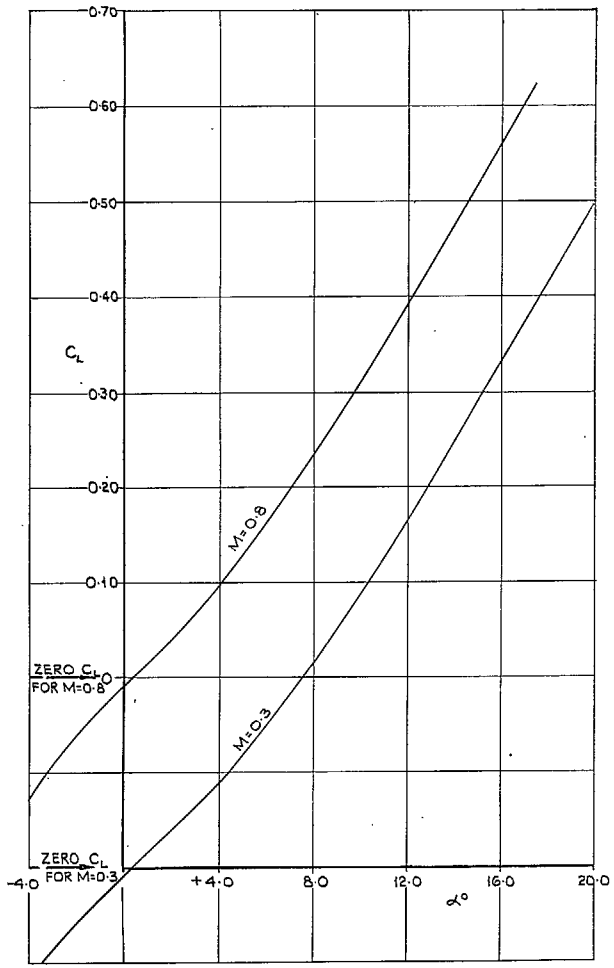

FIG. 11. Variation of C_L with α at subsonic speeds, results for basic nose with or without fin.

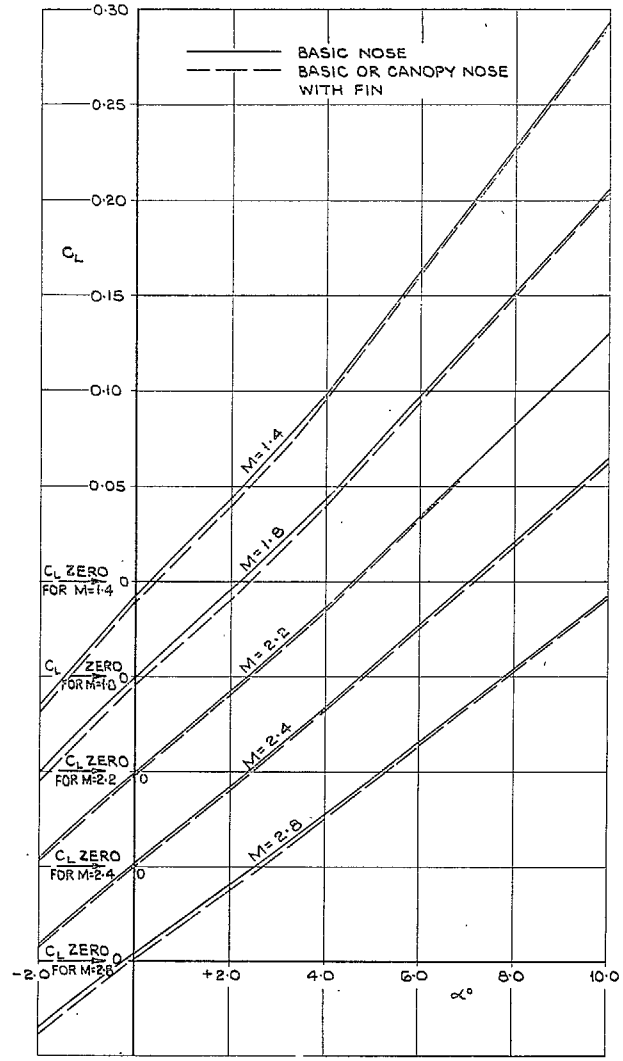

FIG. 12. Effect of fin and canopy on the variation of C_L with α at supersonic speeds.

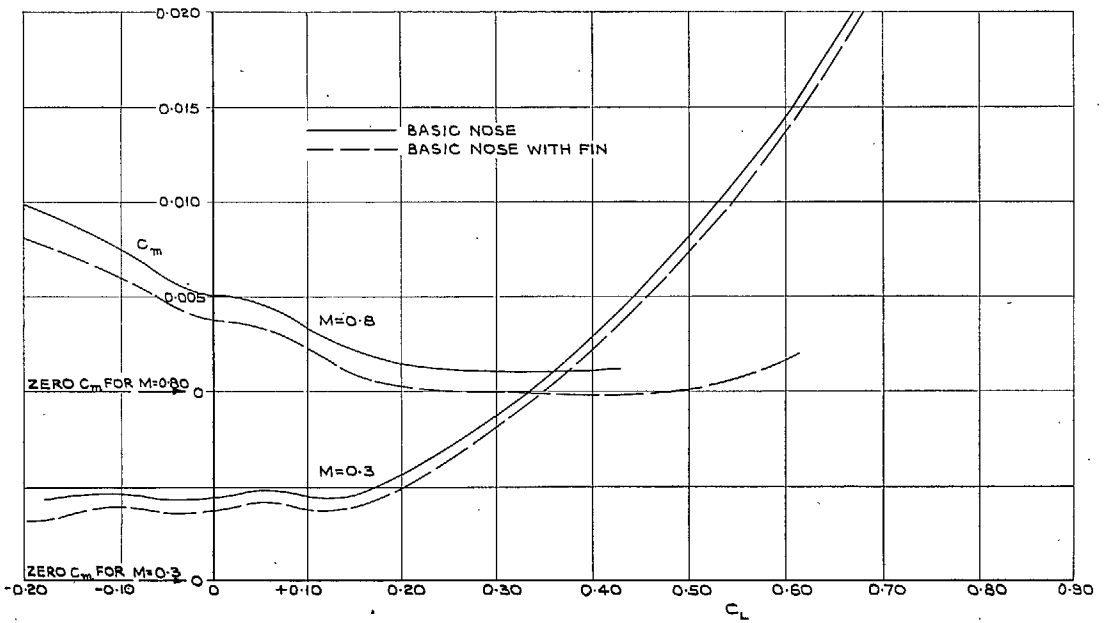

FIG. 13. Variation of C_m with C_L at subsonic speeds.

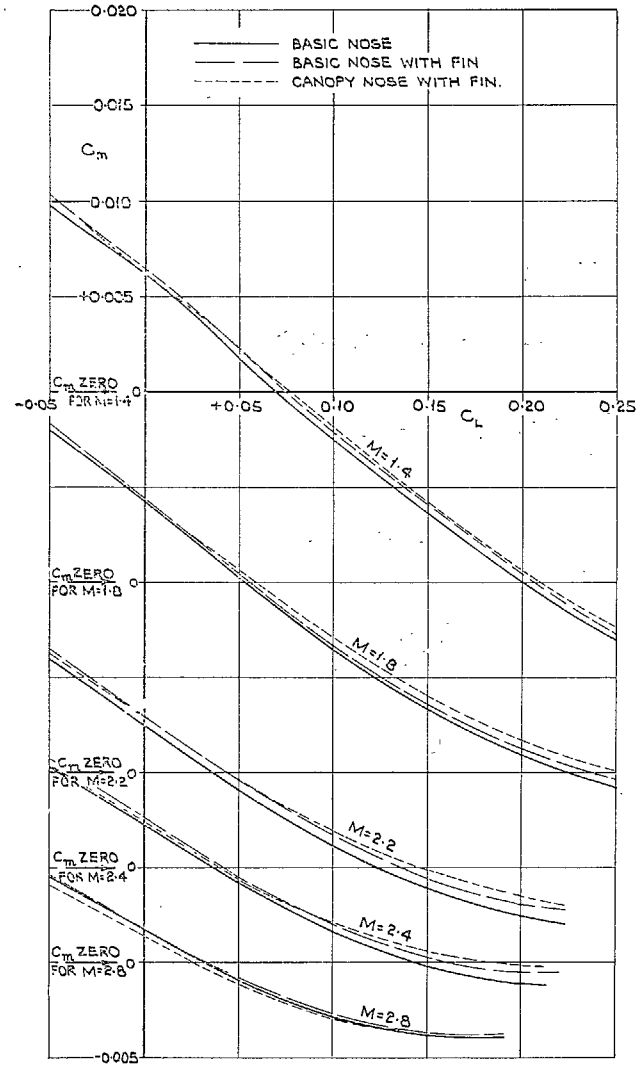

FIG. 14. Effect of fin and canopy on the variation of C_m with C_L at supersonic speeds.

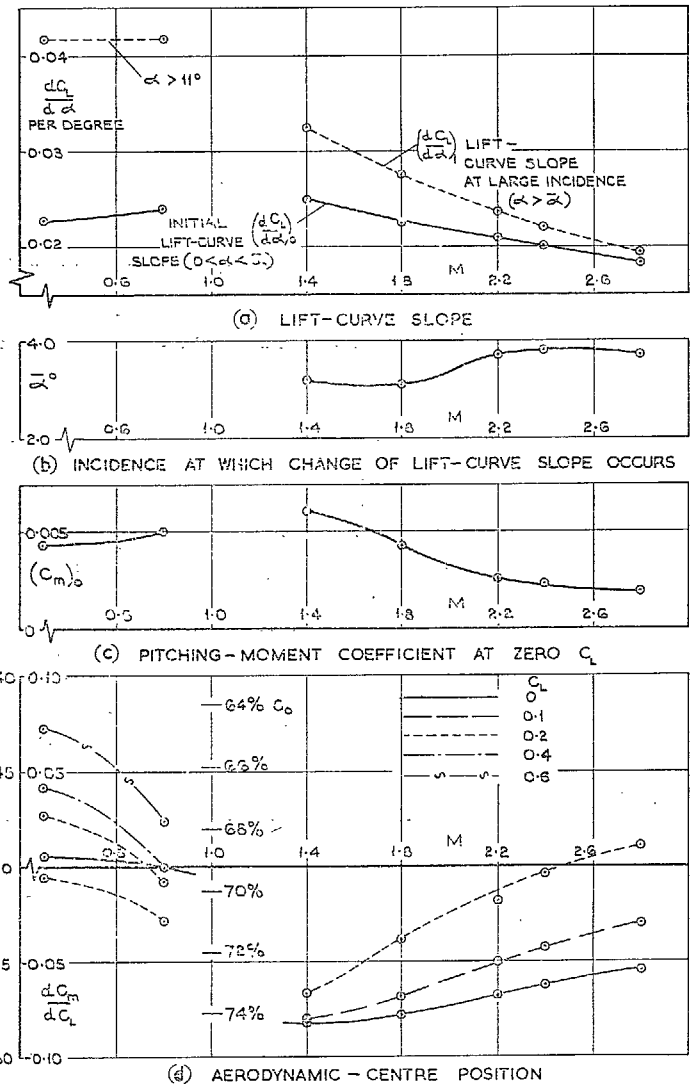

FIG. 15. Basic nose results; variation with Mach number of $dC_L/d\alpha$, $\bar{\alpha}$, $(C_m)_{C_L=0}$ and dC_m/dC_L.

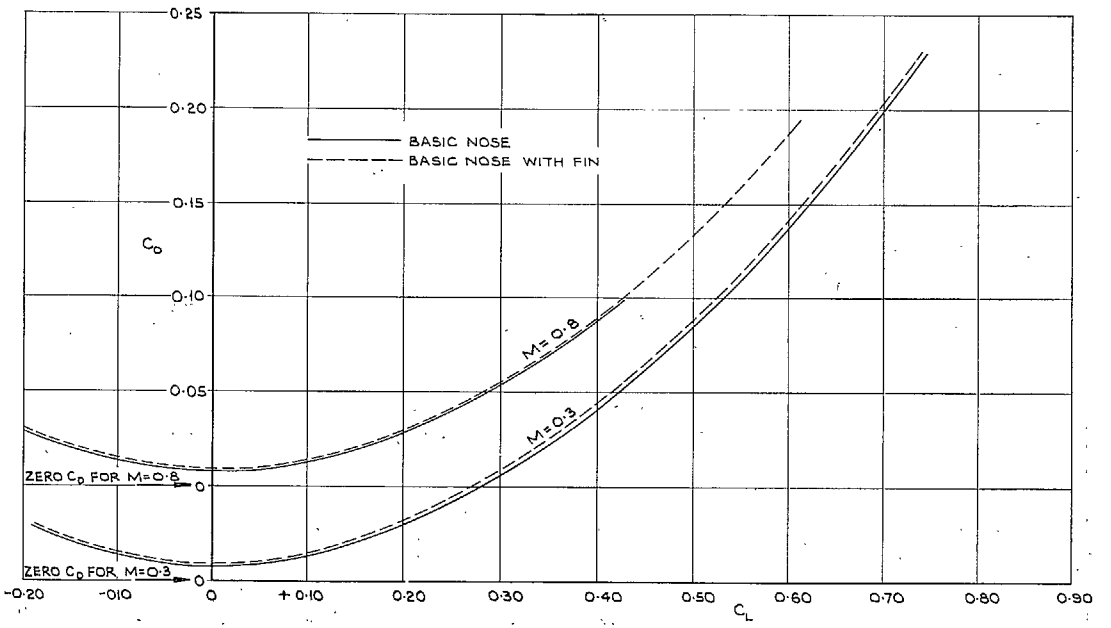

FIG. 16. Variation of C_D with C_L at subsonic speeds.

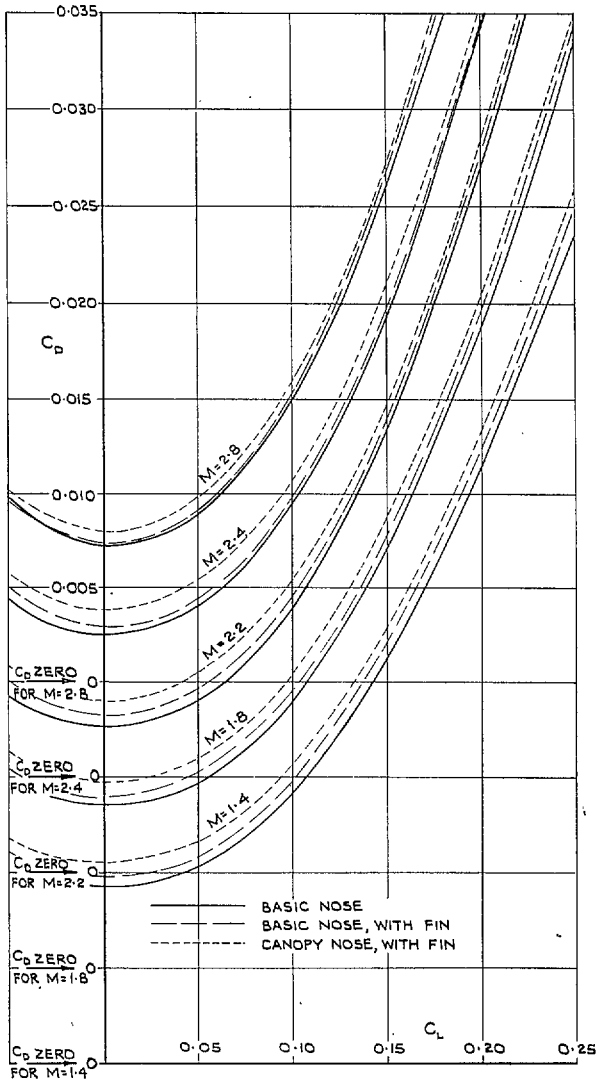

FIG. 17. Effect of fin and canopy on the variation of C_D with C_L at supersonic speeds.

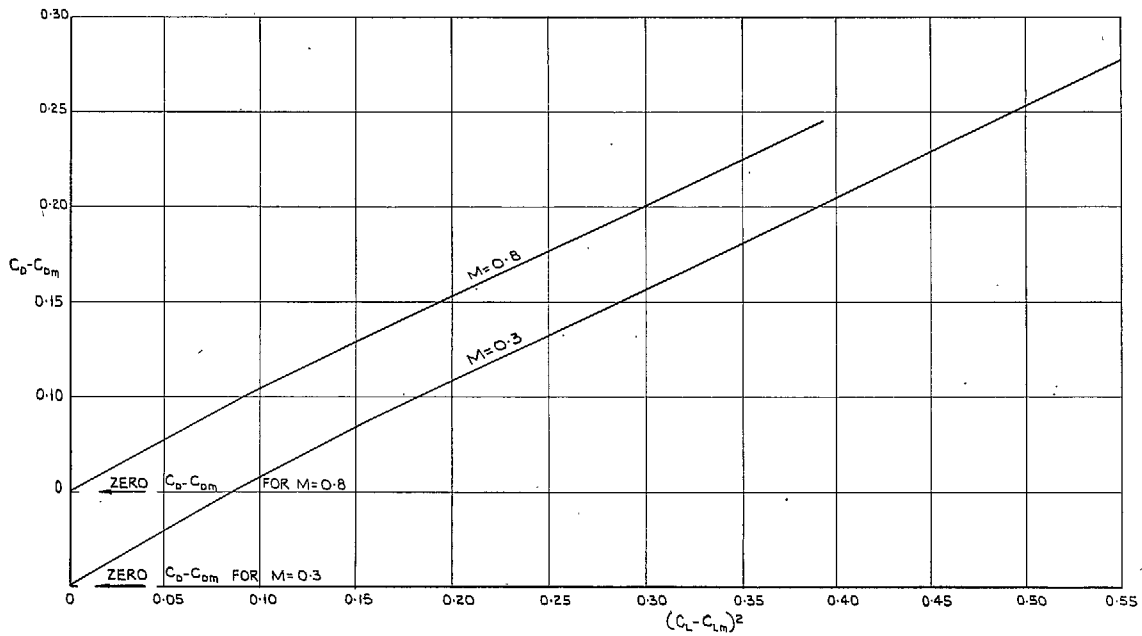

FIG. 18. Variation of $(C_D-C_{D\,m})$ with $(C_L-C_{L\,m})^2$ at subsonic speeds; results for basic nose, with or without fin.

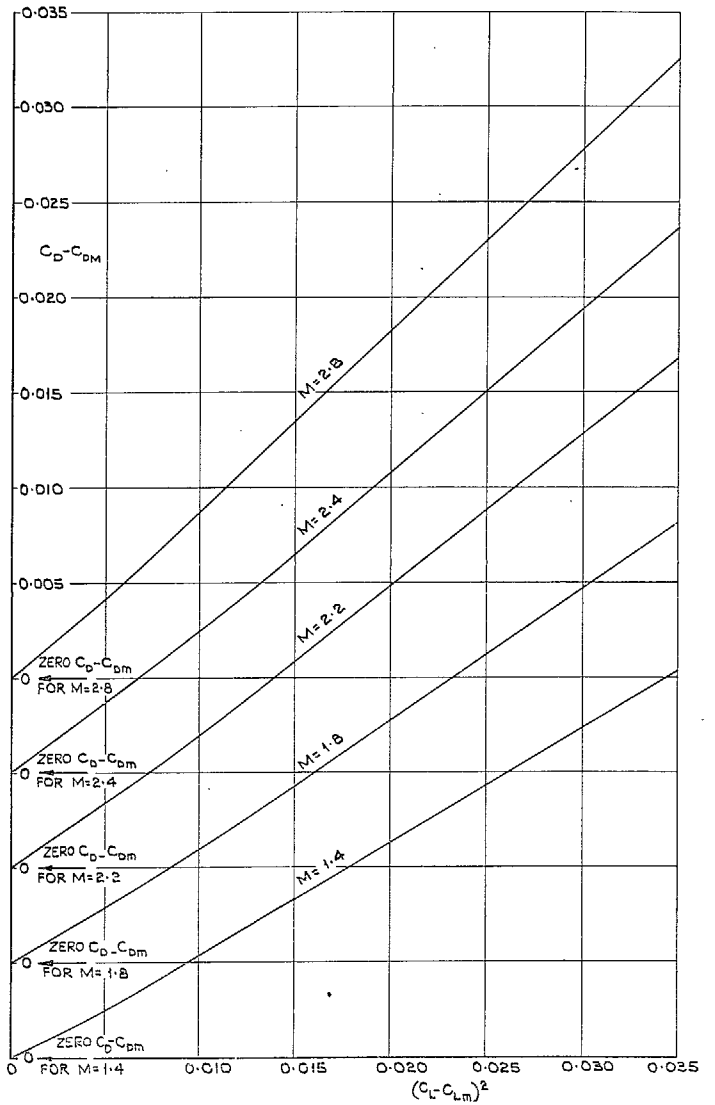

FIG. 19. Variation of $(C_D-C_{D\,m})$ with $(C_L-C_{L\,m})^2$ at supersonic speeds for the basic nose configuration.

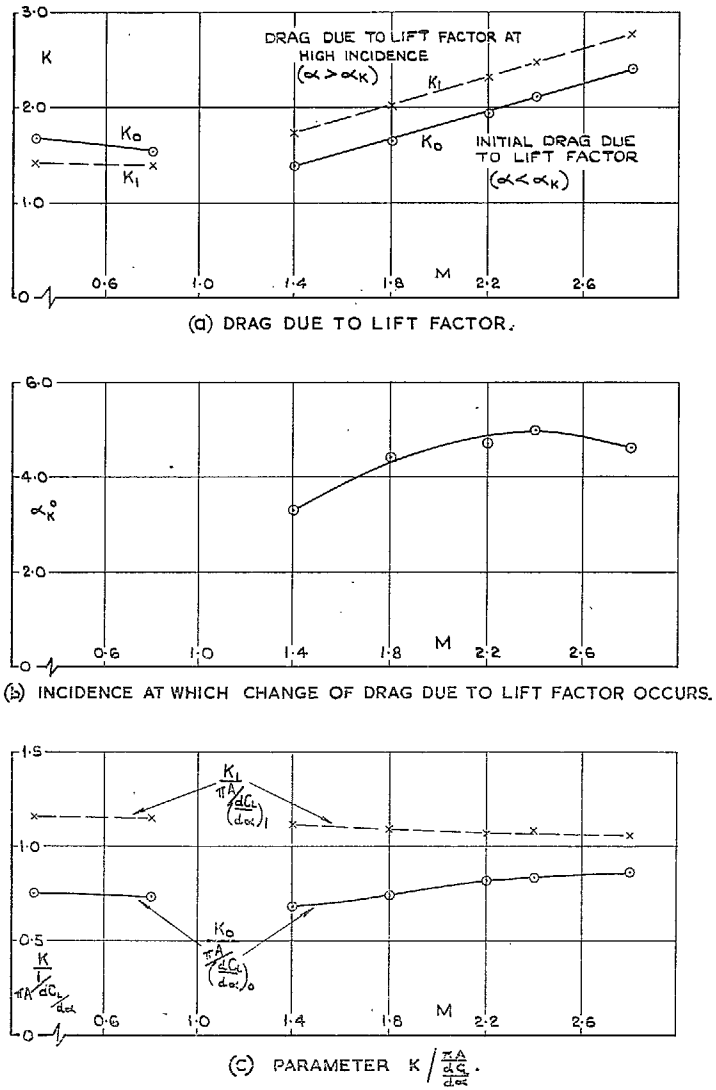

FIG. 20. Basic nose results; variation with Mach number of K, α_K and $K/\pi A/(dC_L/d\alpha)$.

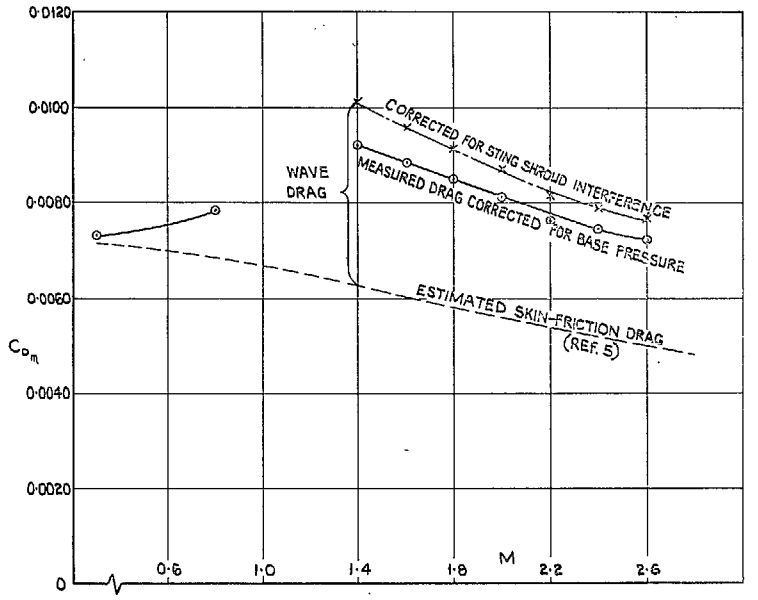

(a) MINIMUM DRAG COEFFICIENT.

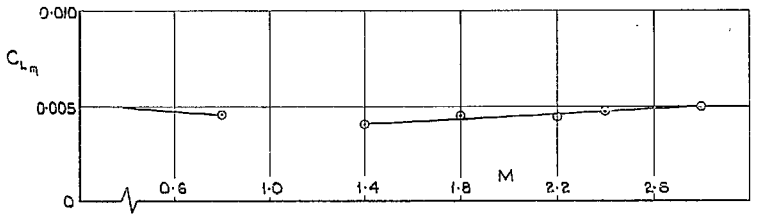

(b) LIFT COEFFICIENT AT MINIMUM DRAG.

FIG. 21. Basic nose results; variation with Mach number of $C_{D\,m}$ and $C_{L\,m}$.

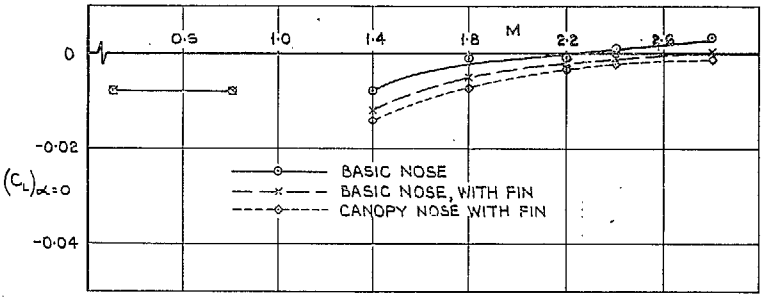

(a) LIFT COEFFICIENT AT ZERO INCIDENCE.

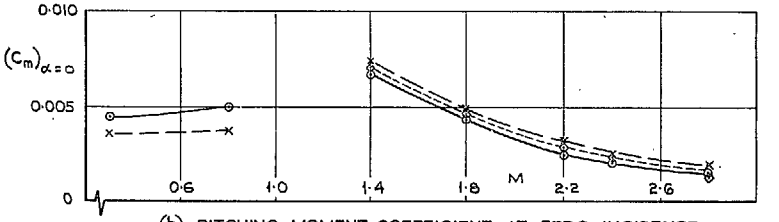

(b) PITCHING-MOMENT COEFFICIENT AT ZERO INCIDENCE.

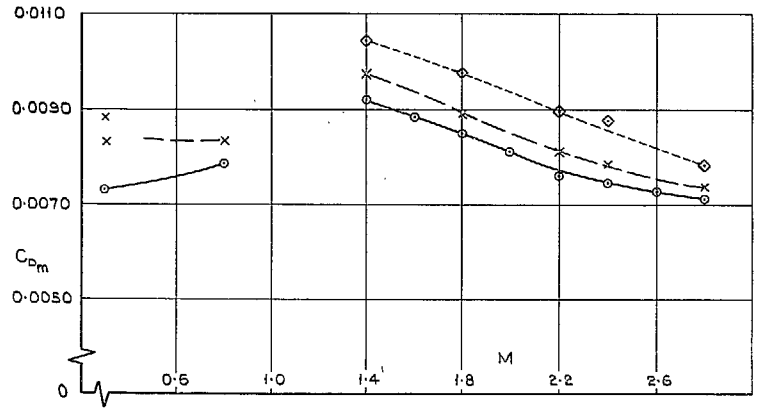

(c) MINIMUM DRAG COEFFICIENT.

FIG. 22. Effect of fin and canopy on the derivatives $(C_L)_{\alpha=0}$, $(C_m)_{\alpha=0}$ and $C_{D\,m}$.

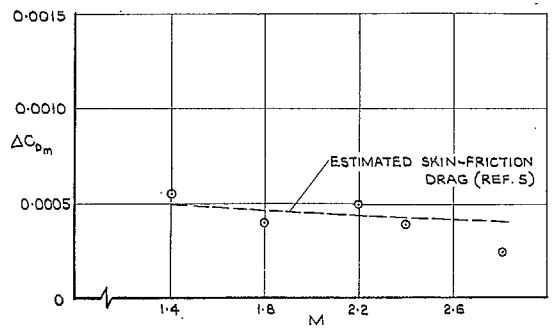

FIG. 23. Drag increment due to the fin.

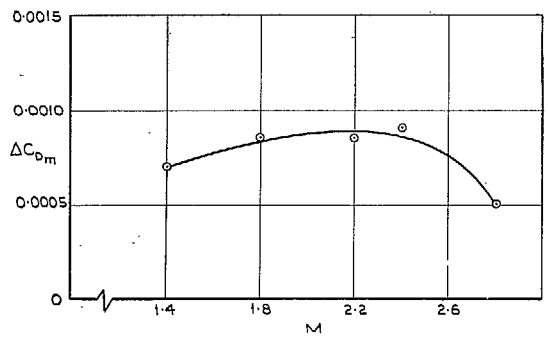

FIG. 24. Drag increment due to the canopy.

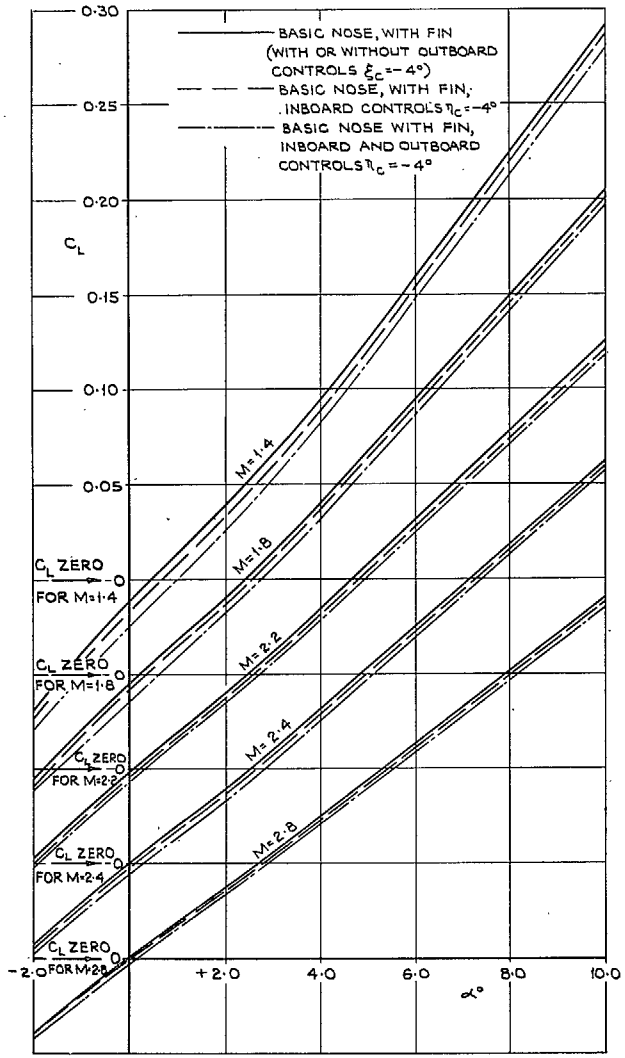

FIG. 25. Effect of control deflection on the variation of C_L with α at supersonic speeds.

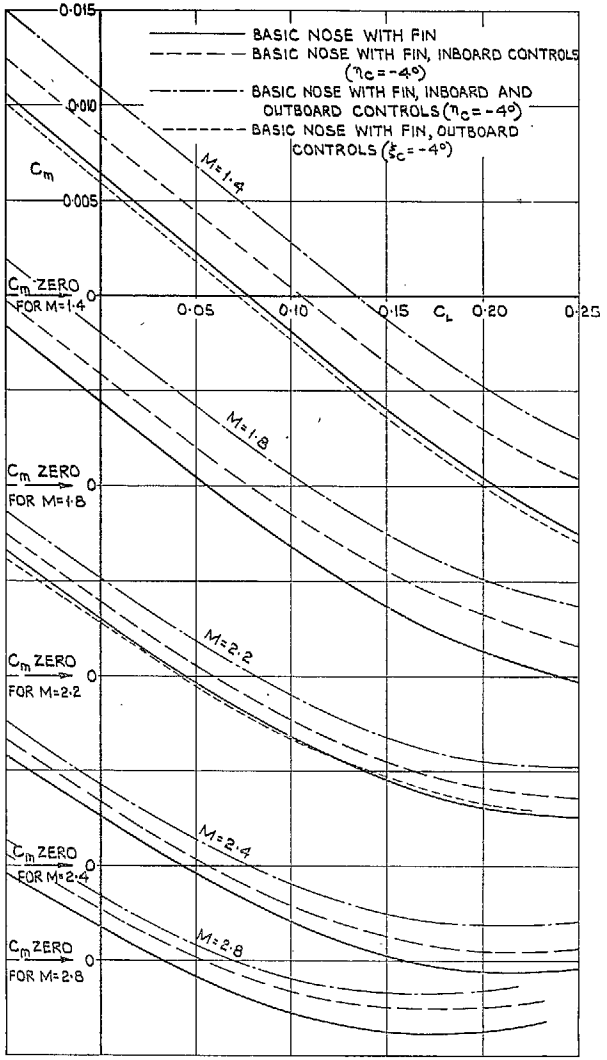

FIG. 26. Effect of control deflection on the variation of C_m with C_L at supersonic speeds.

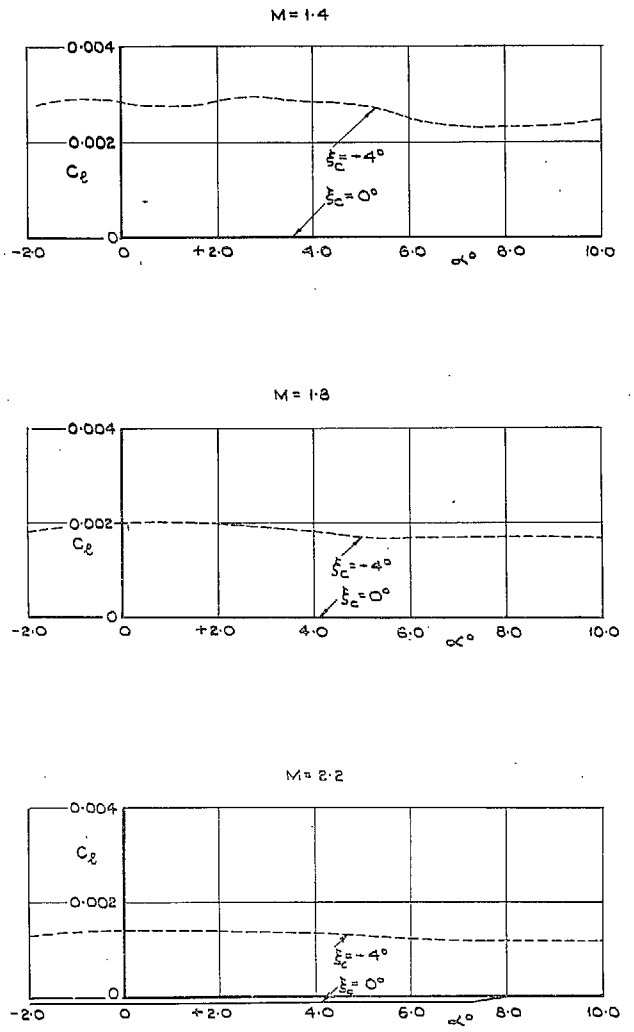

FIG. 27. Effect of control deflection on the variation of C_l with α at supersonic speeds; basic nose, with fin.

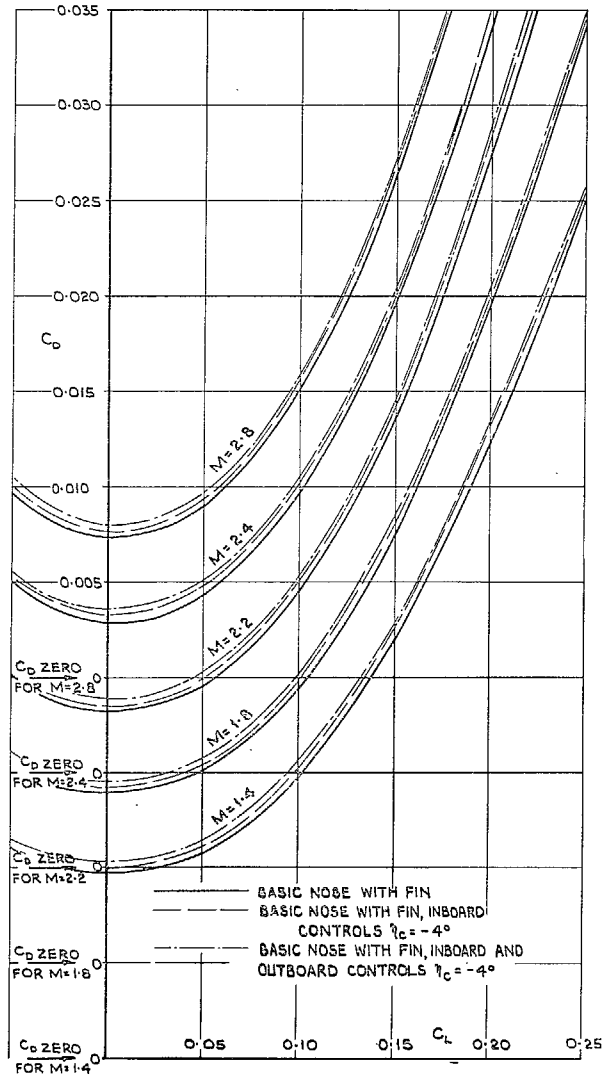

FIG. 28a. Effect of control deflection on the variation of C_D with C_L at supersonic speeds.

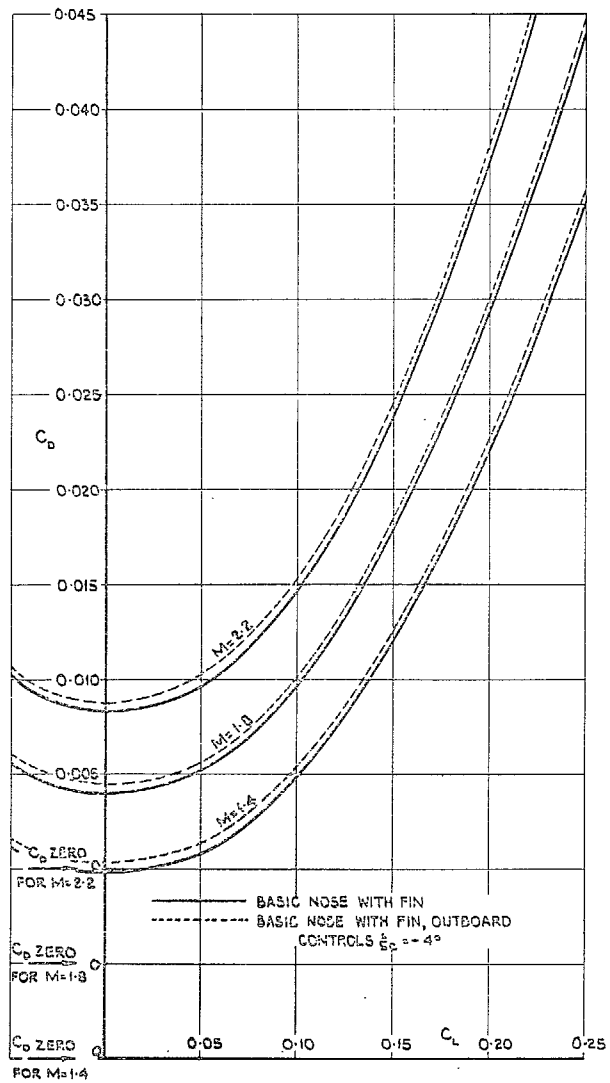

FIG. 28b. Effect of control deflection on the variation of C_D with C_L at supersonic speeds.

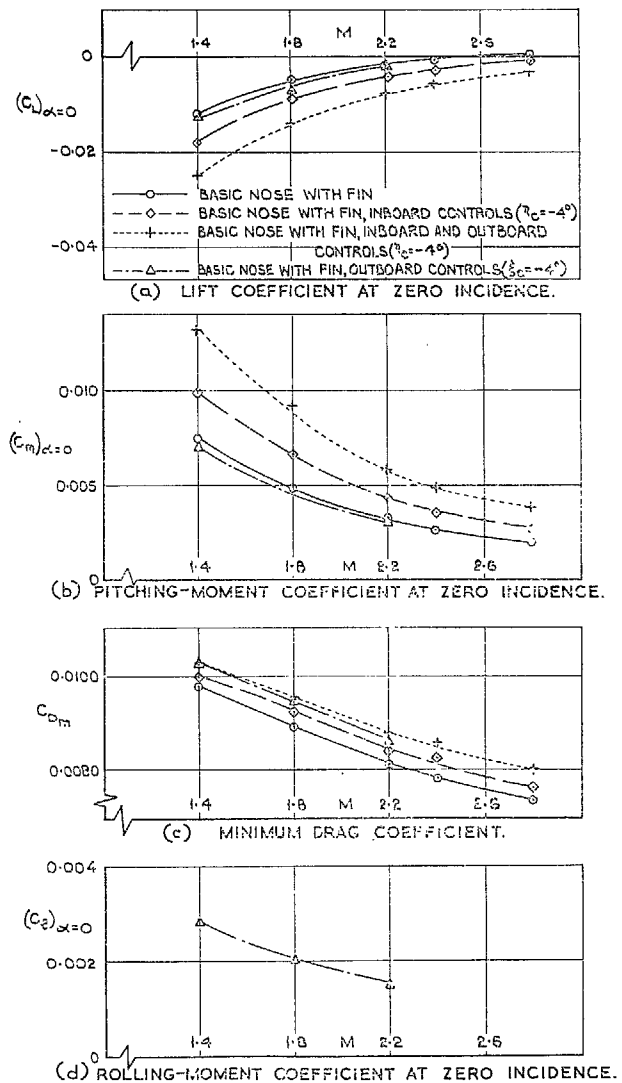

FIG. 29. Effect of control deflection on $(C_L)_{\alpha=0}$, $(C_m)_{\alpha=0}$, $C_{D\,m}$ and $(C_l)_{\alpha=0}$.

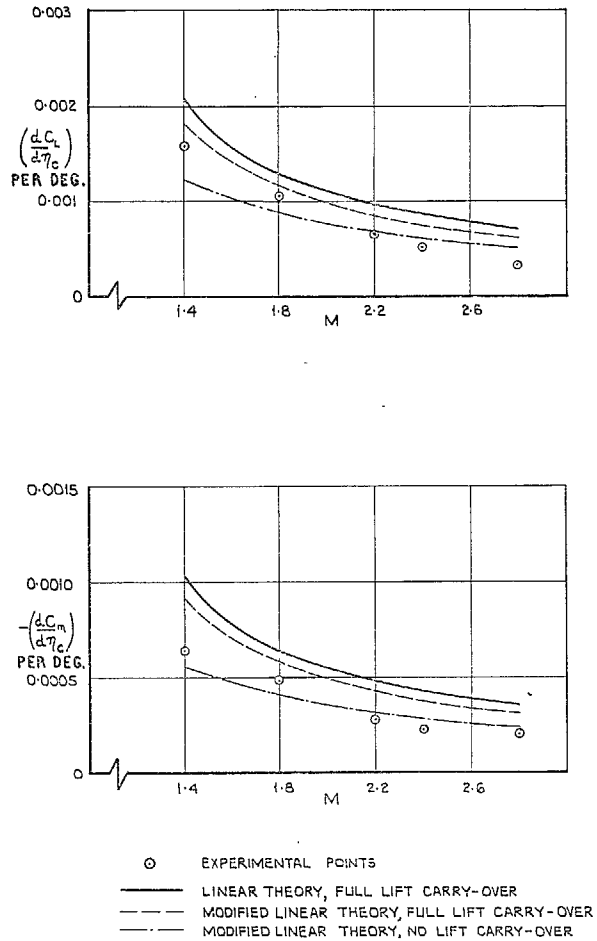

FIG. 30. Effectiveness of inboard controls as elevators; $\alpha = 0$.

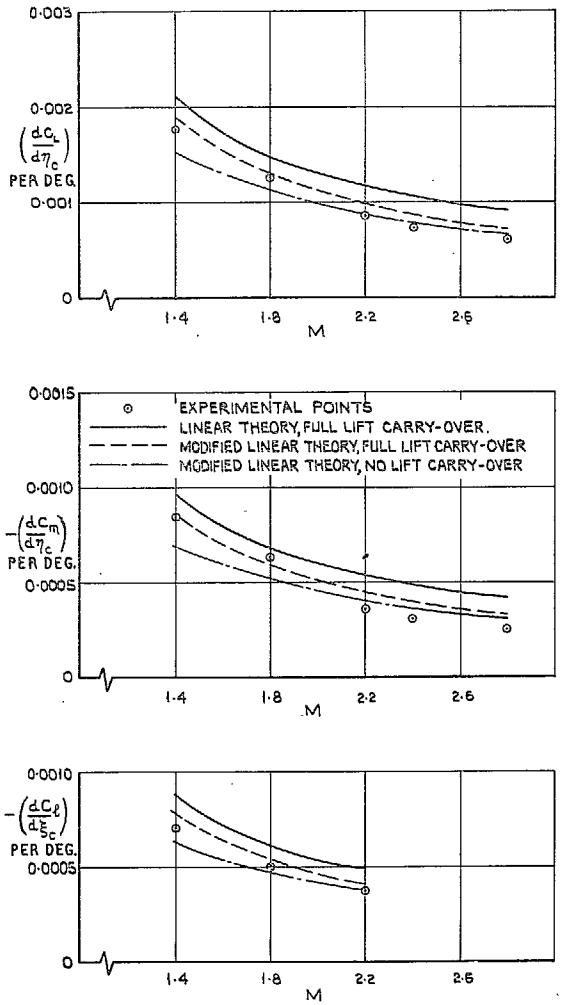

FIG. 31. Effectiveness of outboard controls as elevators and ailerons; $\alpha = 0$.

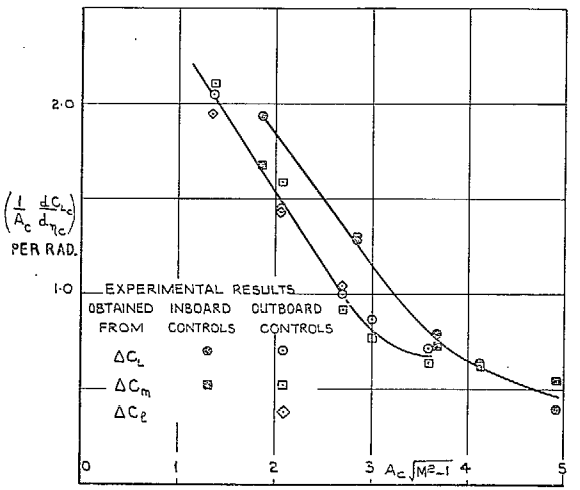

FIG. 32. Variation of $1/A_c\ dC_{Lc}/d\eta_c$ with $A_c\sqrt{(M^2-1)}$ for the controls; inboard control results not corrected for shroud interference.

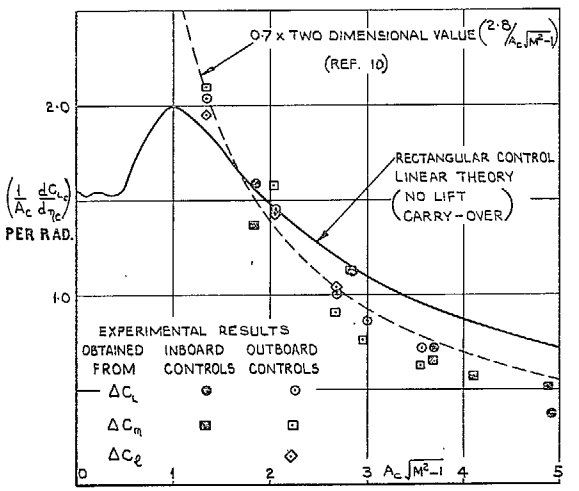

FIG. 33. Variation of $1/A_c\ dC_{Lc}/d\eta_c$ with $A_c\sqrt{(M^2-1)}$ for the controls; inboard control results corrected for shroud interference.

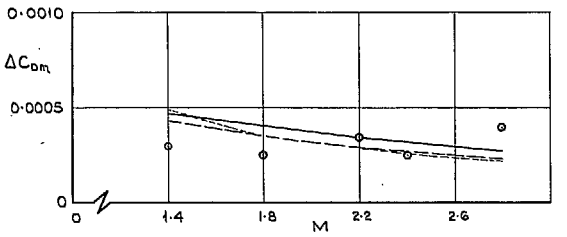

(a) OUTBOARD CONTROLS.

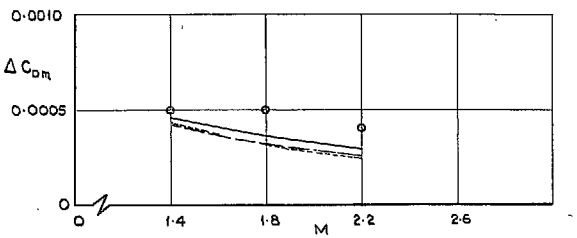

(b) OUTBOARD CONTROLS (AS AILERONS).

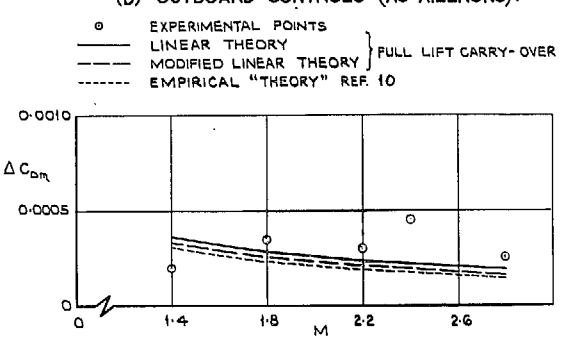

(c) INBOARD CONTROLS.

FIG. 34. Increment in minimum drag due to the controls; nominal control setting 4°.

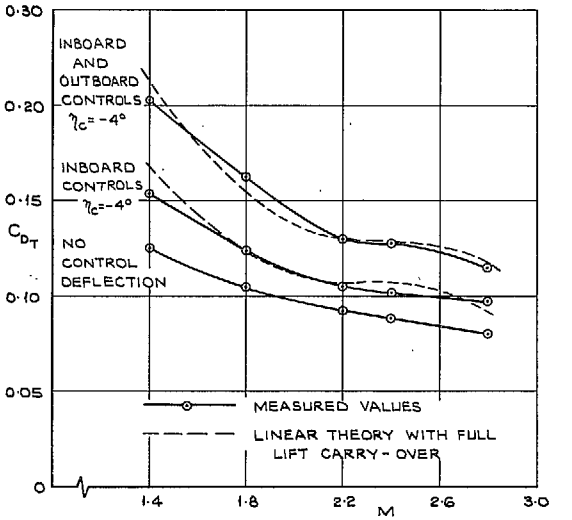

FIG. 35. Drag coefficient of trimmed wing (η_c constant).

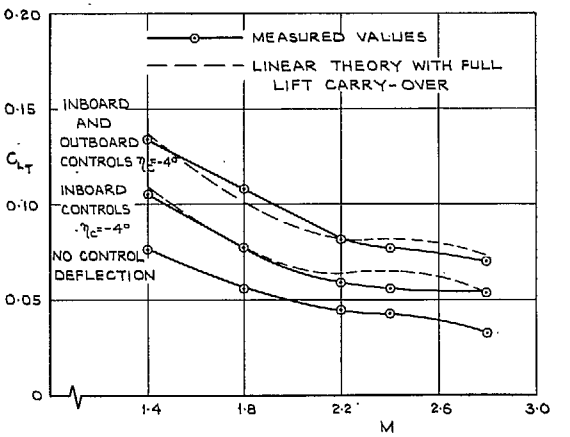

FIG. 36. Lift coefficient of trimmed wing (η_c constant).

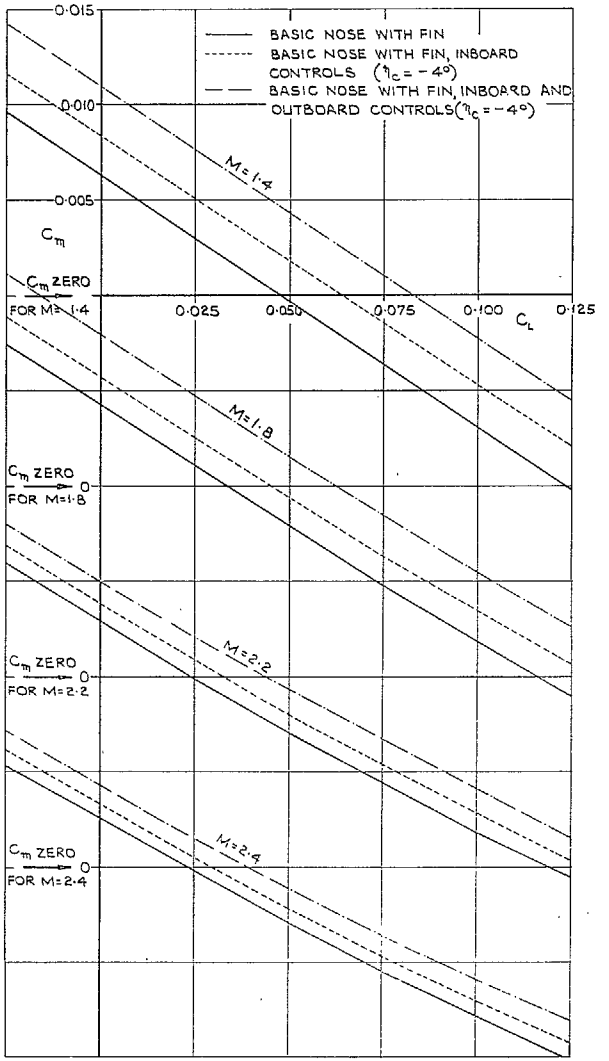

FIG. 37. Variation of C_m with C_L at supersonic speeds; moment reference centre at $0{\cdot}45\ \bar{c}$ to give neutral stability at $M = 0{\cdot}3$, $C_L = 0{\cdot}45$.

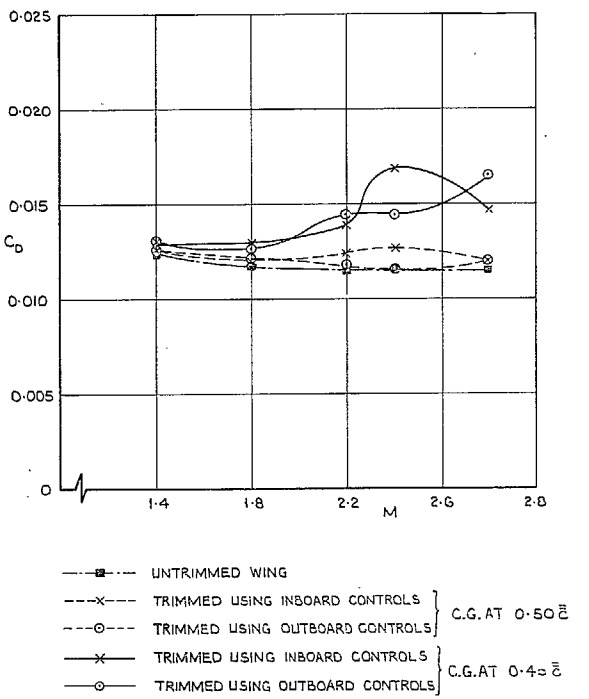

FIG. 38. Drag coefficient of trimmed wing, $C_L = 0{\cdot}075$.

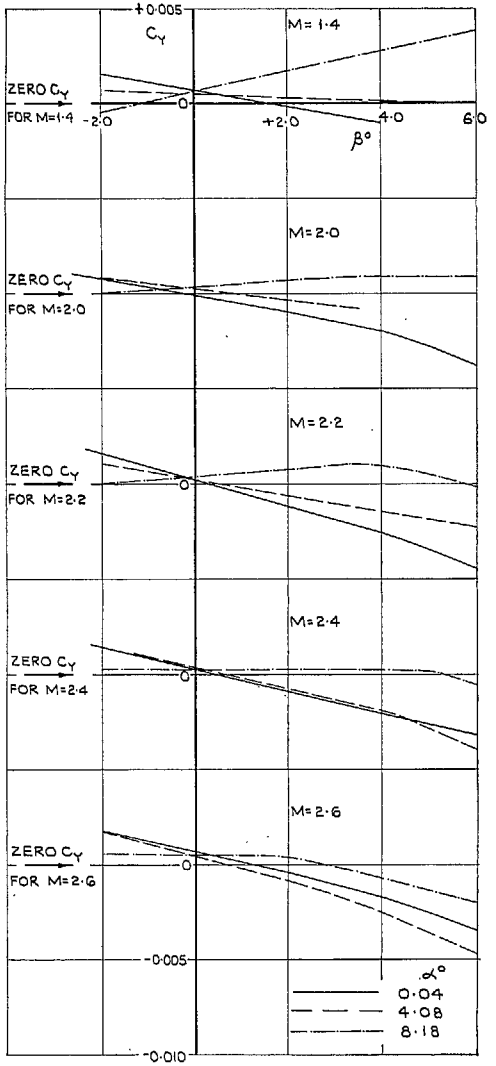

FIG. 39. Variation of C_Y with β at supersonic speeds; basic nose, no fin.

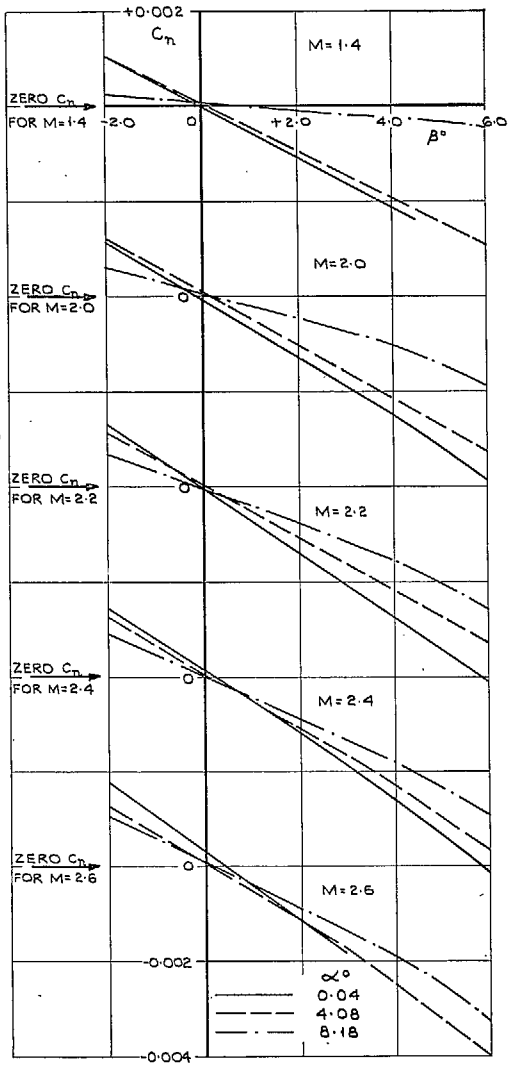

FIG. 40. Variation of C_n with β at supersonic speeds; basic nose, no fin.

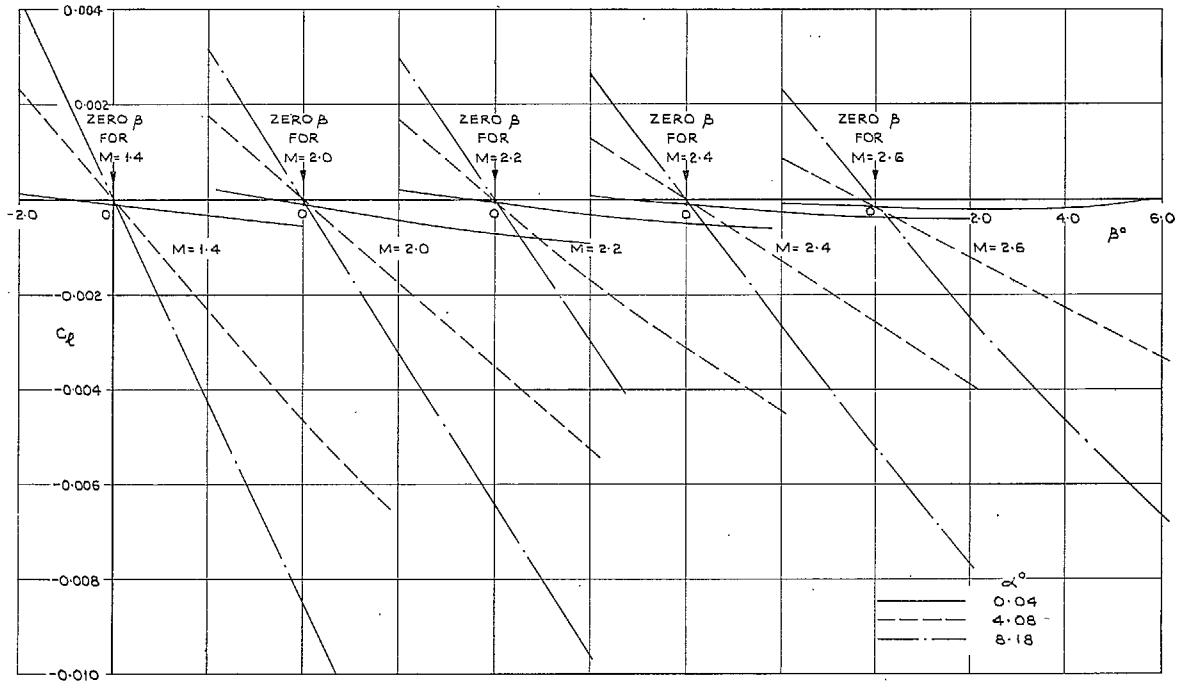

FIG. 41. Variation of C_l with β at supersonic speeds; basic nose, no fin.

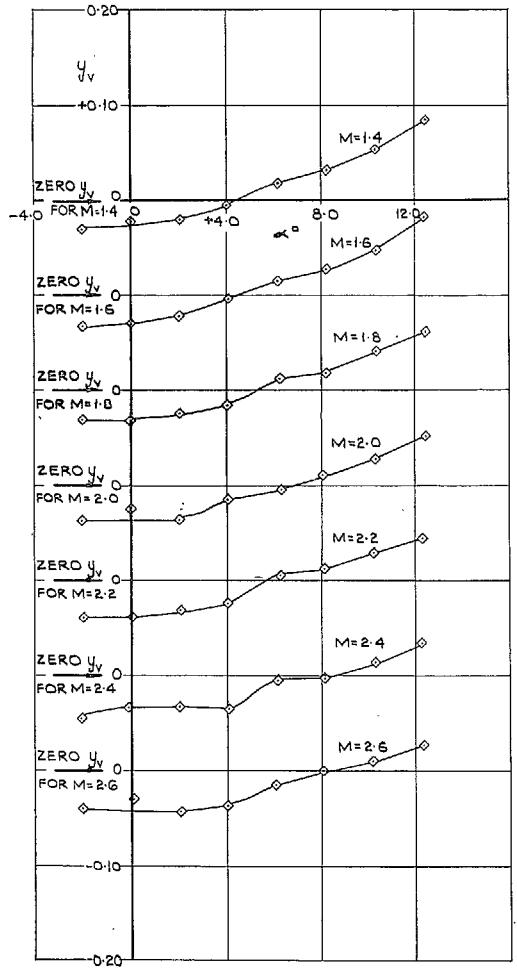

FIG. 42. Variation of y_v with α at supersonic speeds; basic nose, no fin.

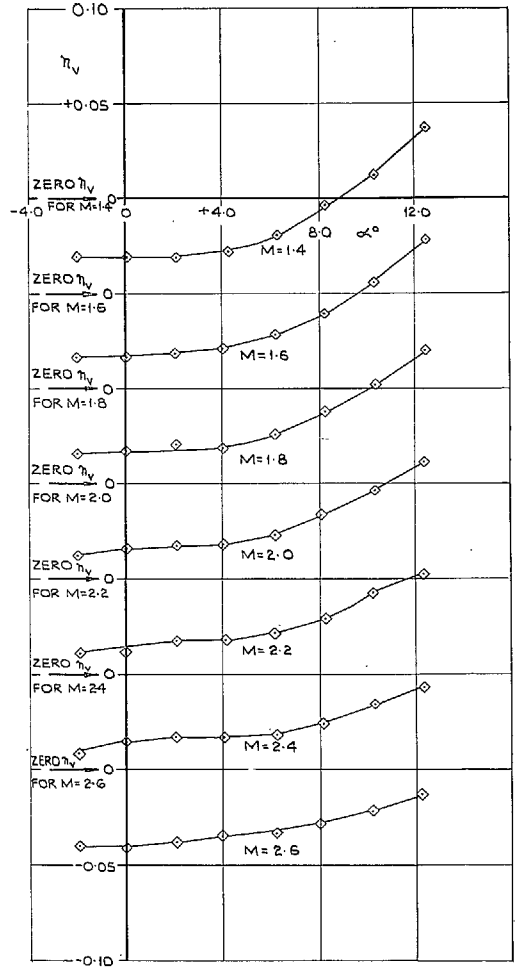

FIG. 43. Variation of n_v with α at supersonic speeds; basic nose, no fin.

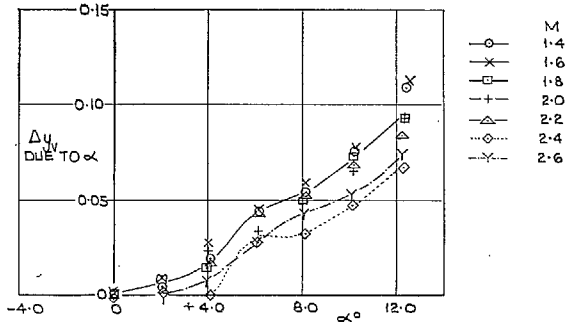

FIG. 44. Incidence dependent y_v ; basic nose, no fin.

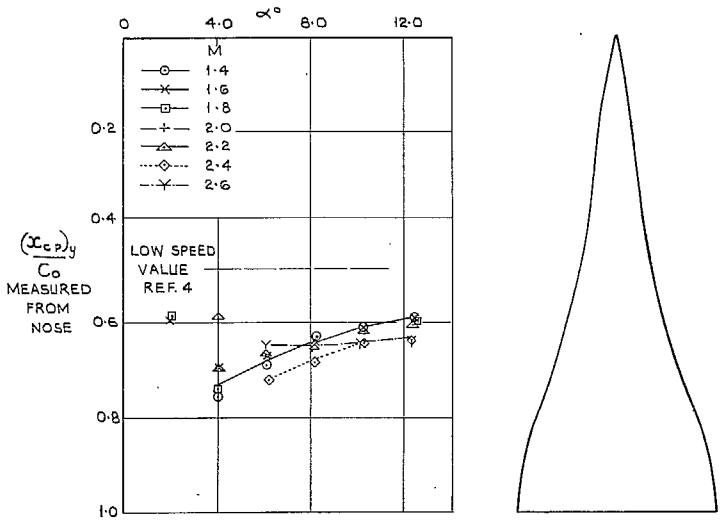

FIG. 45. Chordwise centre-of-pressure position of incidence dependent y_v ; basic nose, no fin.

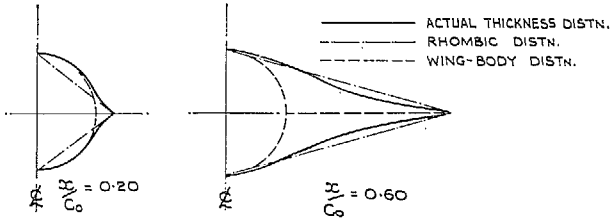

FIG. 46. Comparison between the actual spanwise thickness distributions and the theoretical models.

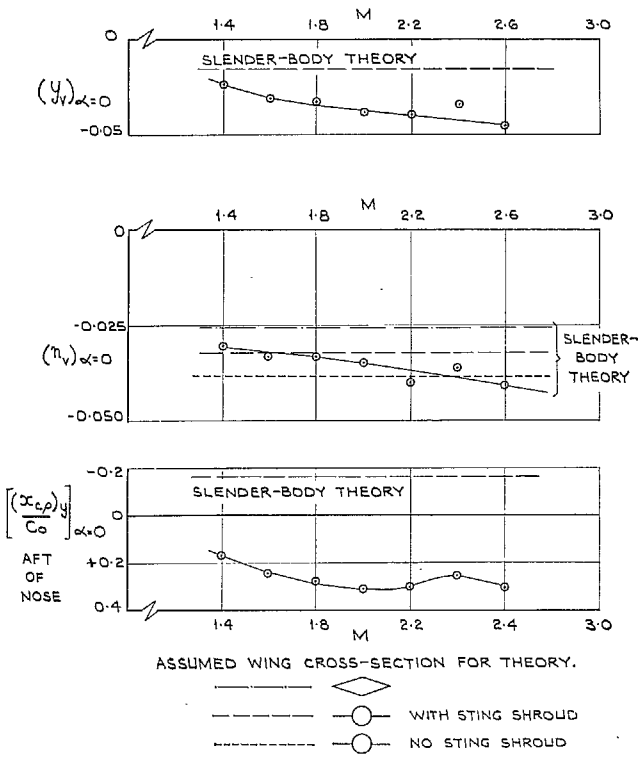

FIG. 47. Comparison with theory, $(y_v)_{\alpha=0}$, $(n_v)_{\alpha=0}$ and $[(x_{C.P.})y/c_0]_{\alpha=0}$; basic nose, no fin.

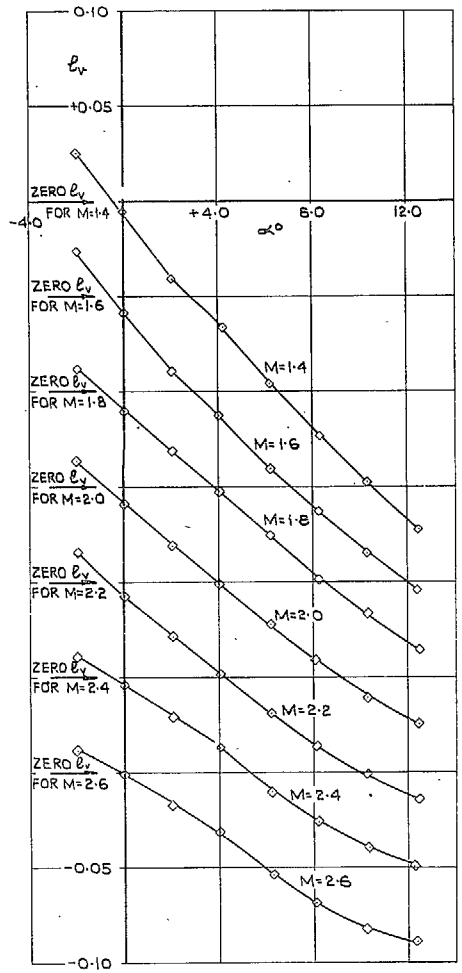

FIG. 48. Variation of l_v with α at supersonic speeds; basic nose, no fin.

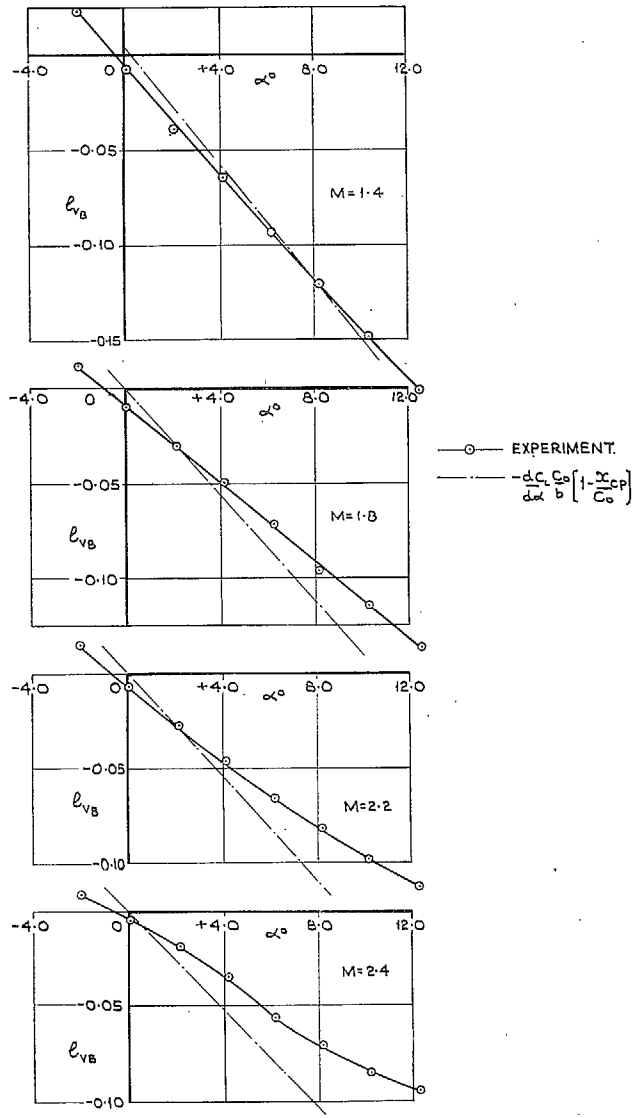

FIG. 49. Comparison with theory, l_{v_B} at supersonic speeds; basic nose, no fin.

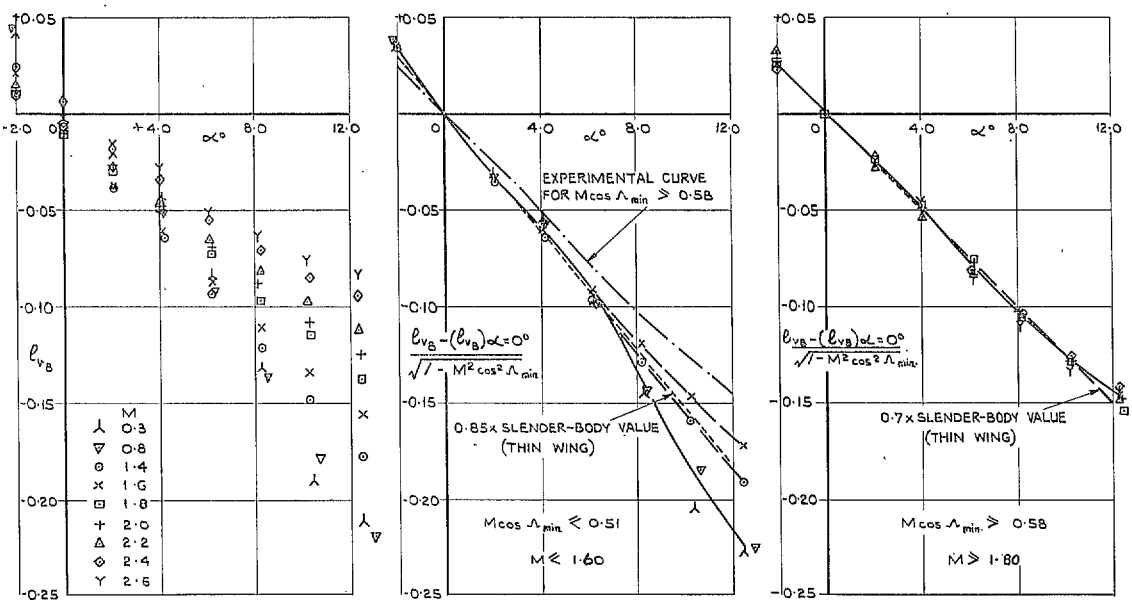

FIG. 50. Variation of $\{l_{v\,B} - (l_{v\,B})_{\alpha=0}\}/(1-M^2\cos^2\Lambda_{\min})^{1/2}$ with α; basic nose, no fin.

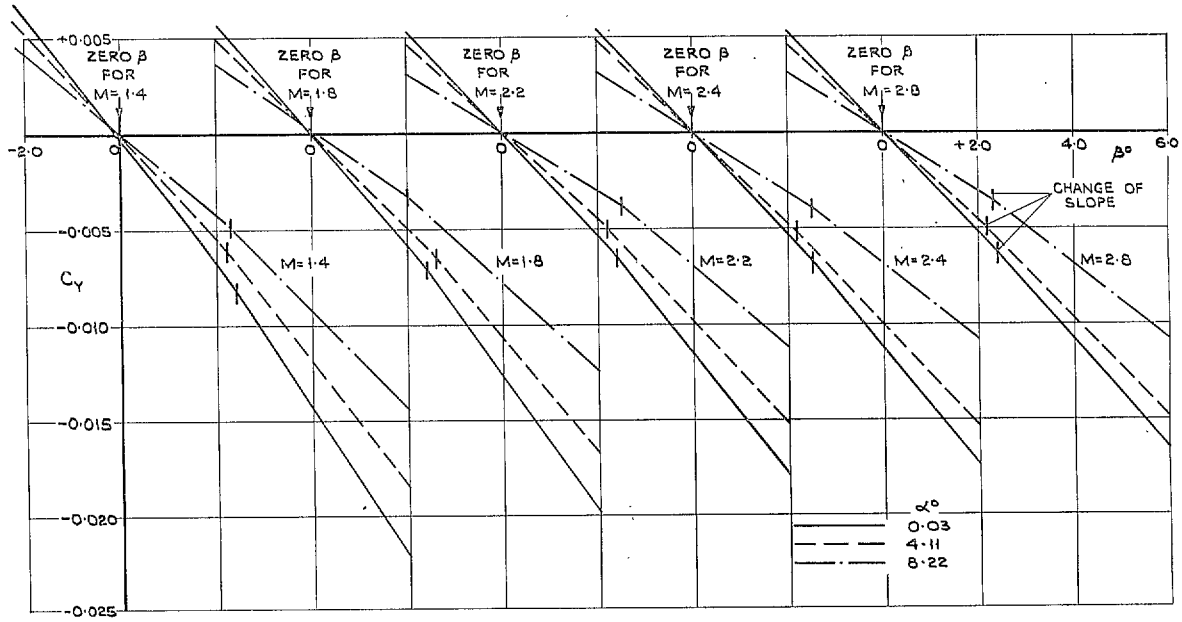

FIG. 51. Variation of C_Y with β at supersonic speeds; basic or canopy nose with fin.

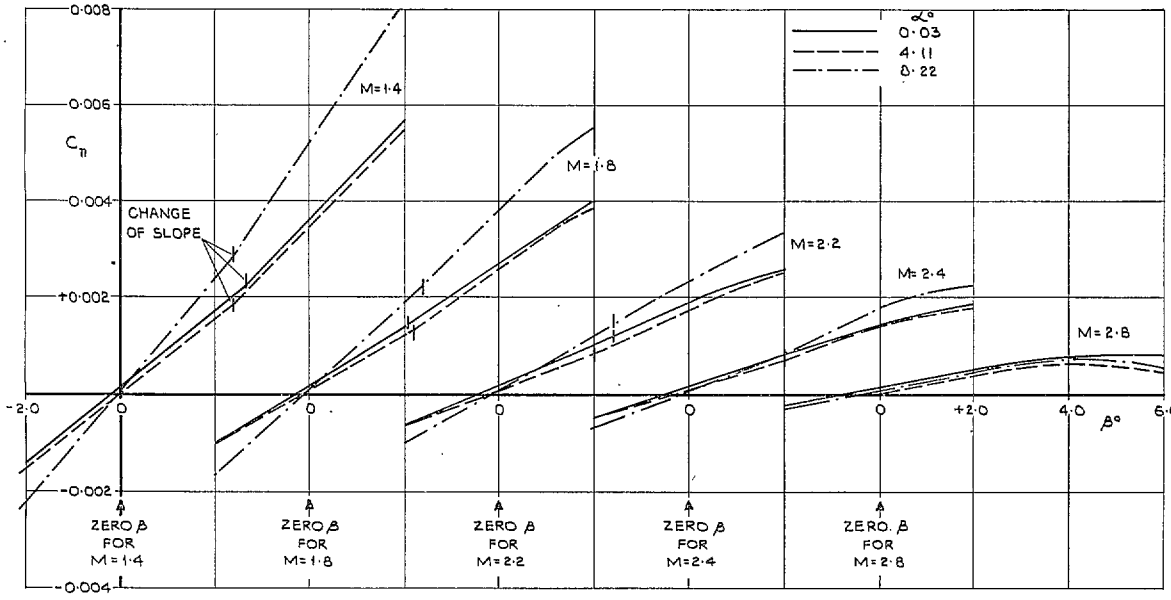

FIG. 52. Variation of C_n with β at supersonic speeds; basic nose, with fin.

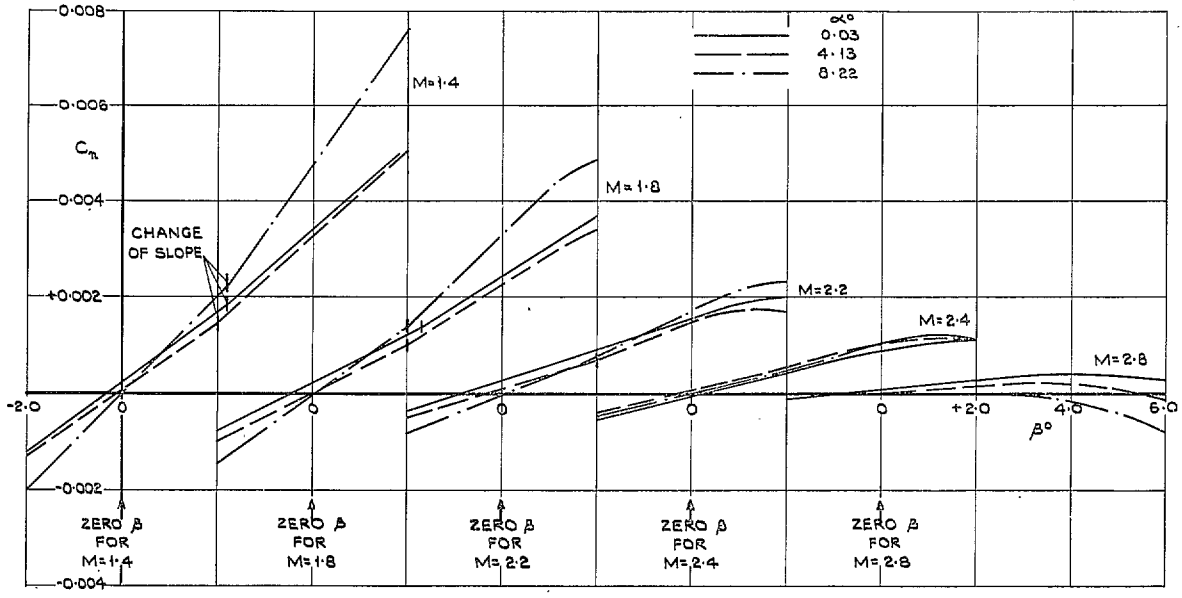

FIG. 53. Variation of C_n with β at supersonic speeds; canopy nose, with fin.

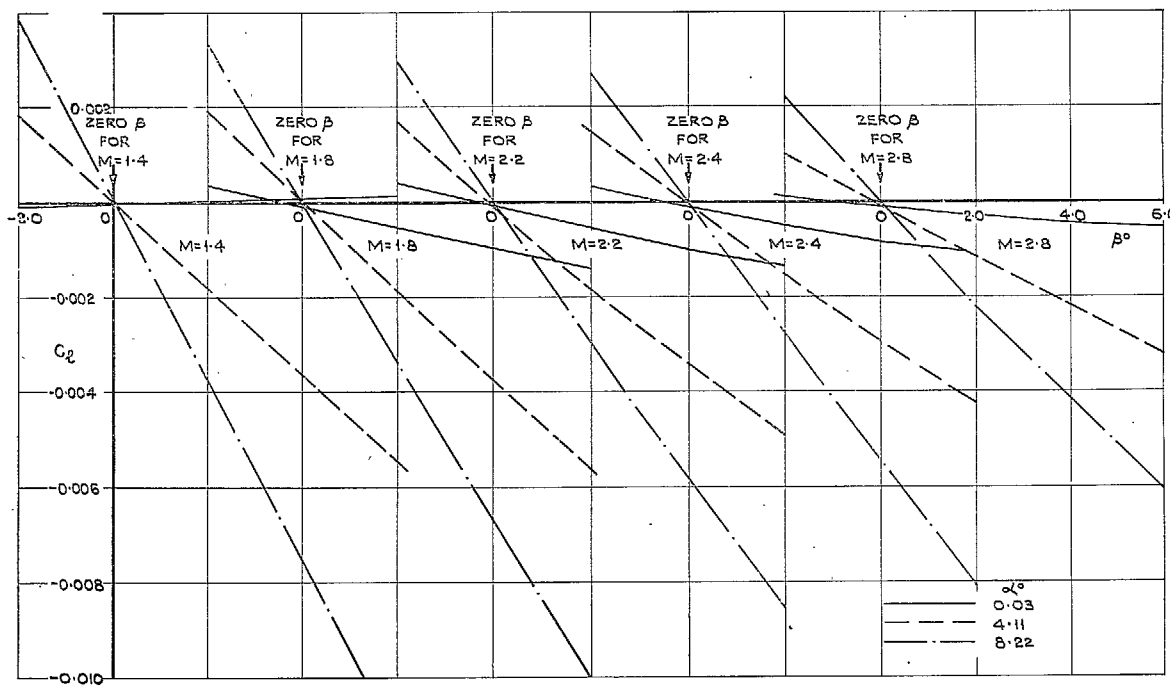

FIG. 54. Variation of C_l with β at supersonic speeds; basic or canopy nose with fin.

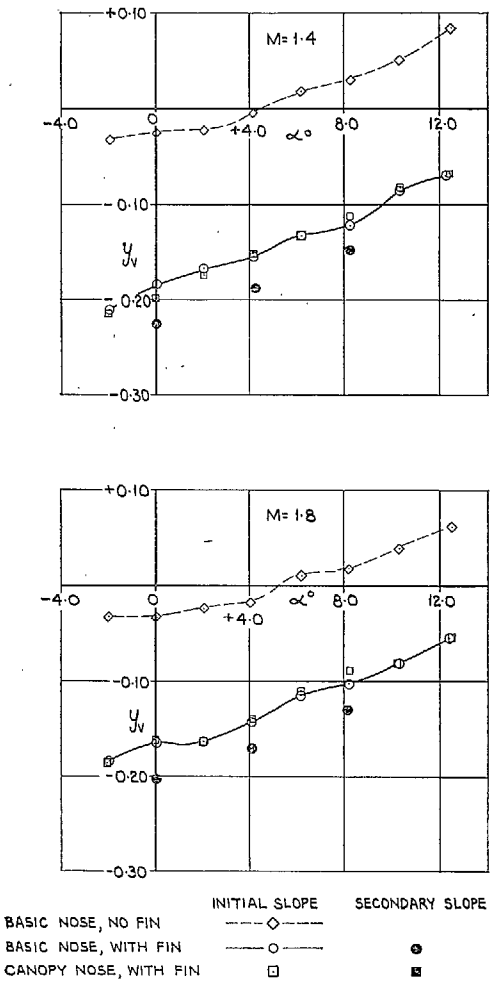

FIG. 55a. Effect of fin and canopy nose on y_v at supersonic speeds.

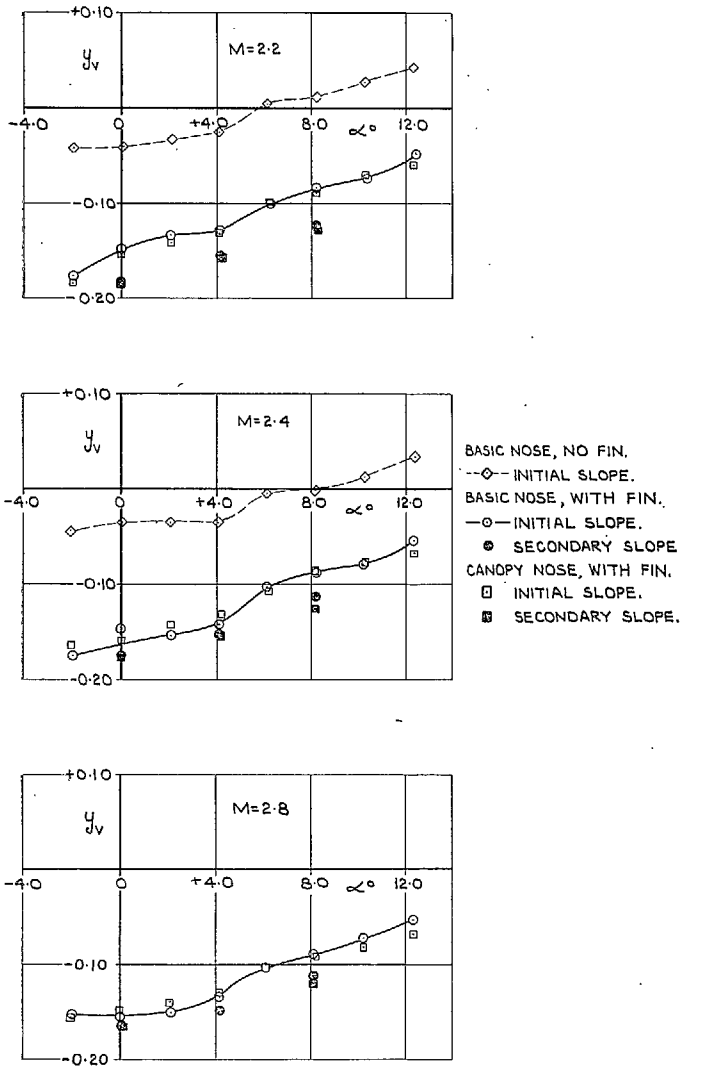

FIG. 55b. Effect of fin and canopy nose on y_v at supersonic speeds.

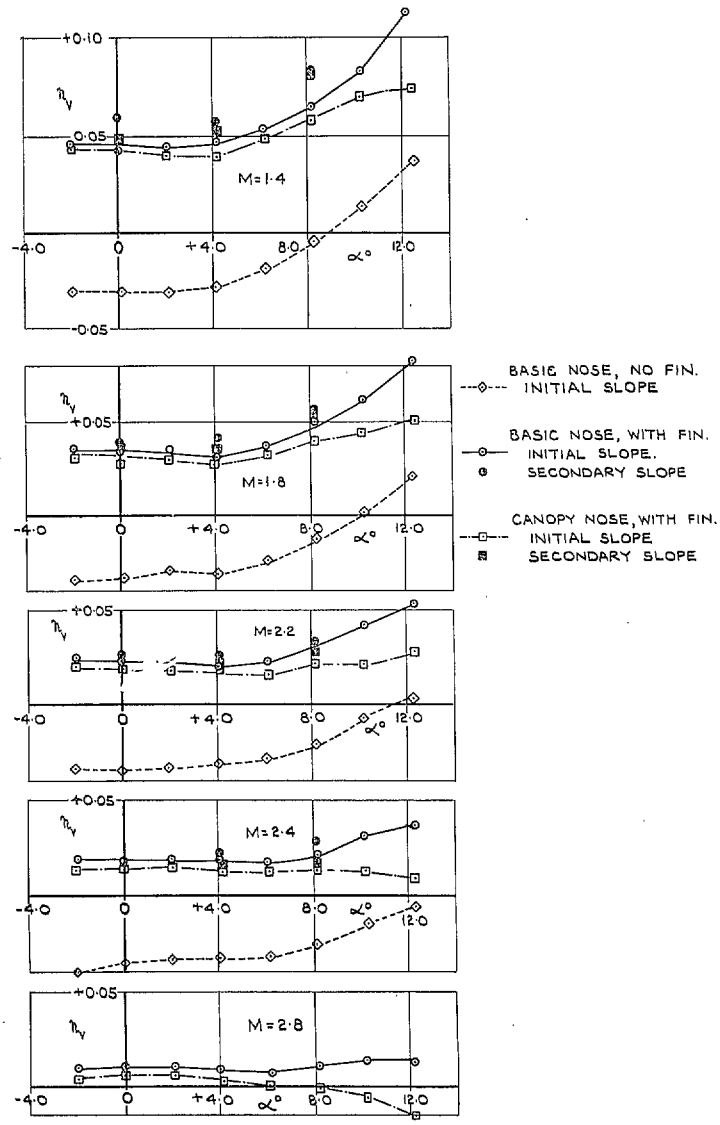

FIG. 56. Effect of fin and canopy nose on n_v at supersonic speeds.

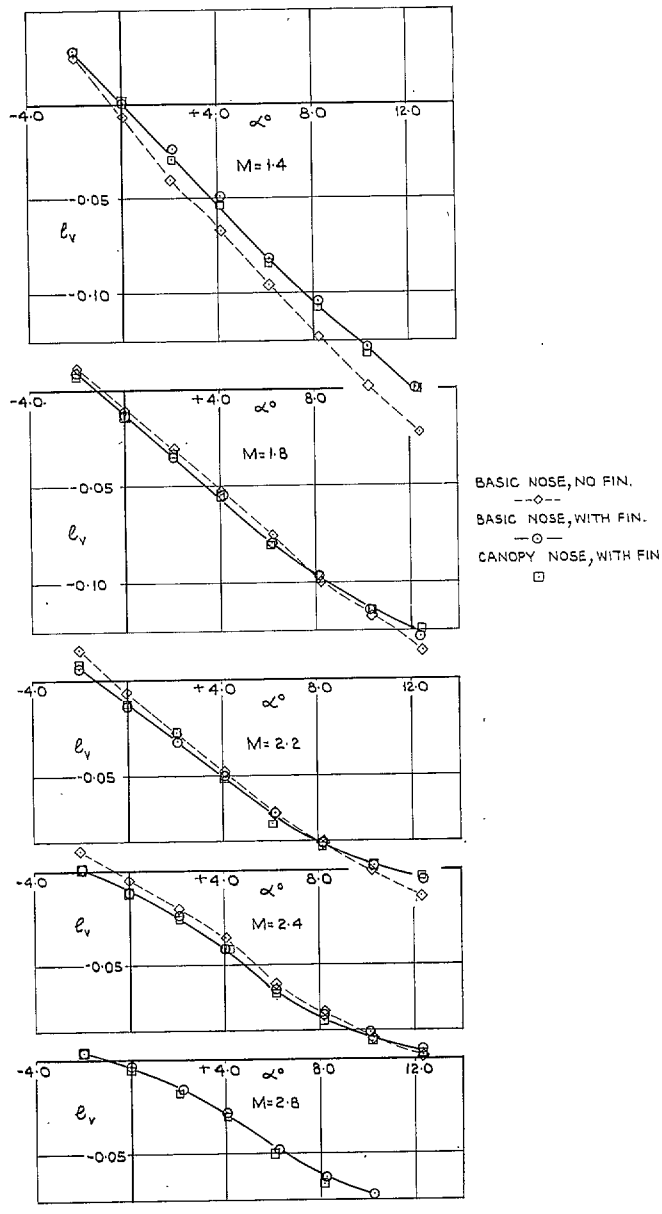

FIG. 57. Effect of fin and canopy nose on l_v at supersonic speeds.

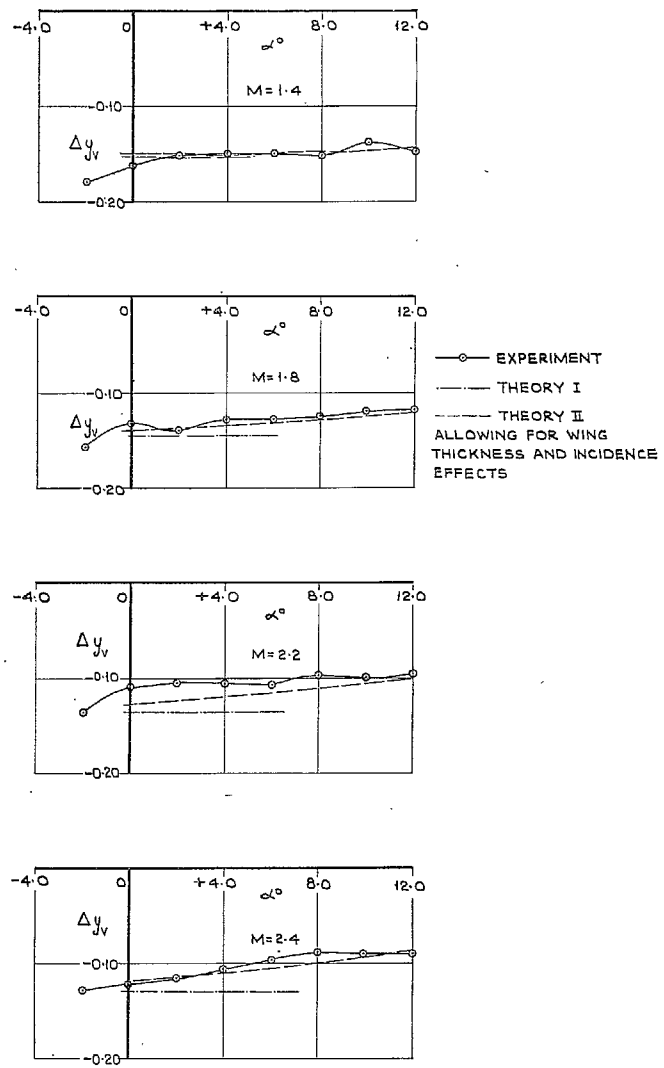

FIG. 58. Fin effectiveness; variation of Δy_v due to fin with α, basic nose.

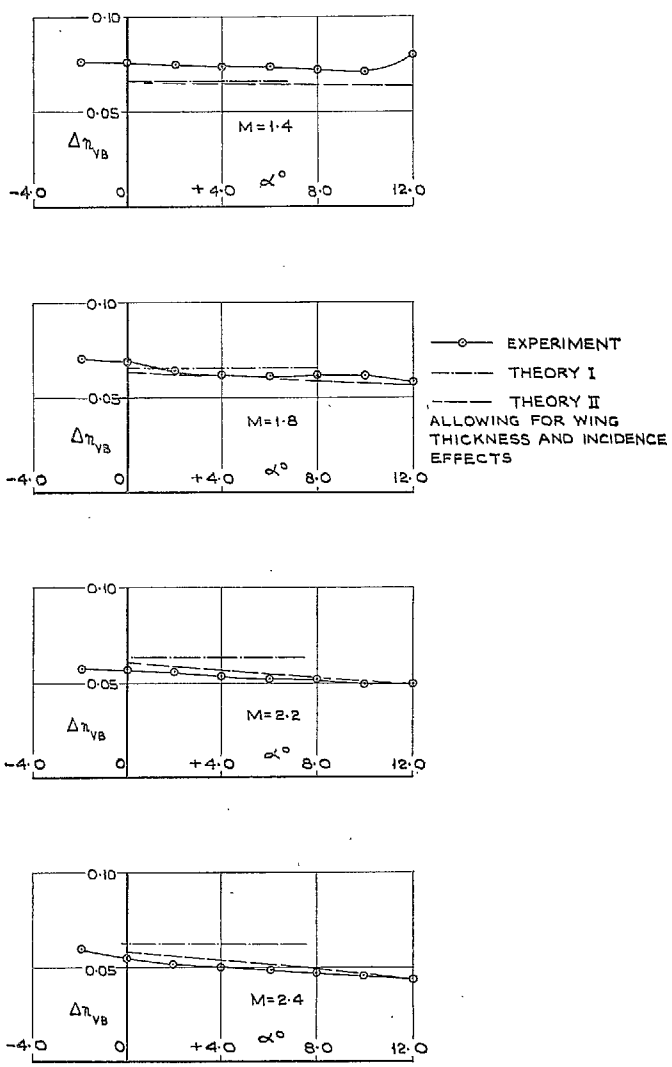

FIG. 59. Fin effectiveness; variation of $\Delta n_{v\,B}$ due to fin with α, basic nose.

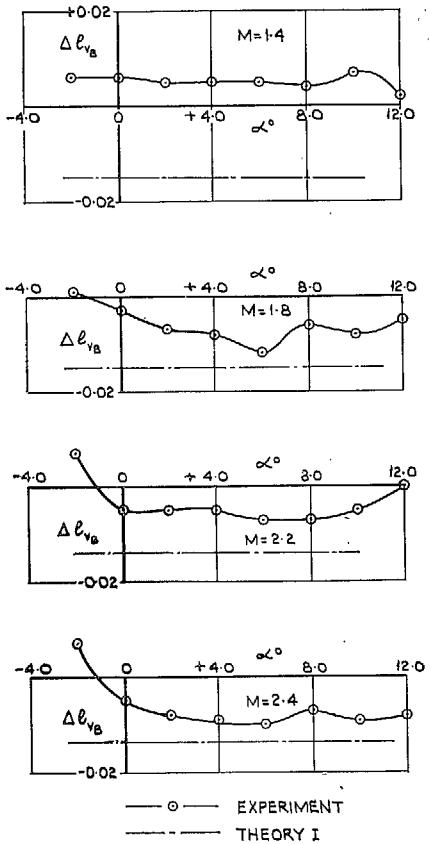

FIG. 60. Fin effectiveness; variation of $\Delta l_{v\,B}$ due to fin with α, basic nose.

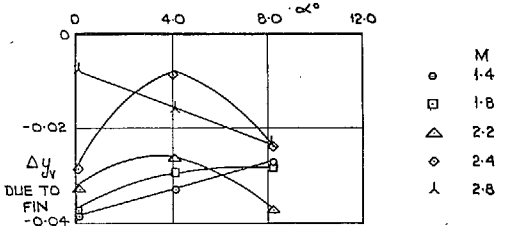

FIG. 61. Sideslip dependent y_v (secondary y_v − initial y_v); basic nose, with fin, supersonic speeds.

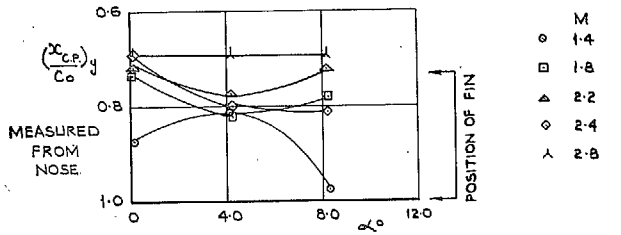

FIG. 62. Chordwise centre-of-pressure position of sideslip dependent y_v; basic nose, with fin, supersonic speeds.

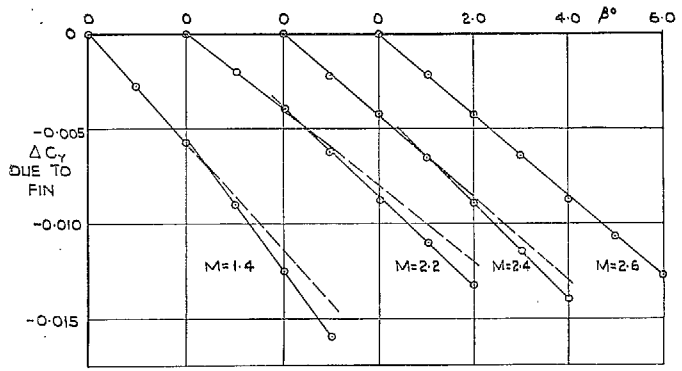

FIG. 63. Variation of ΔC_Y due to the fin with β; basic nose, $\alpha = 0$.

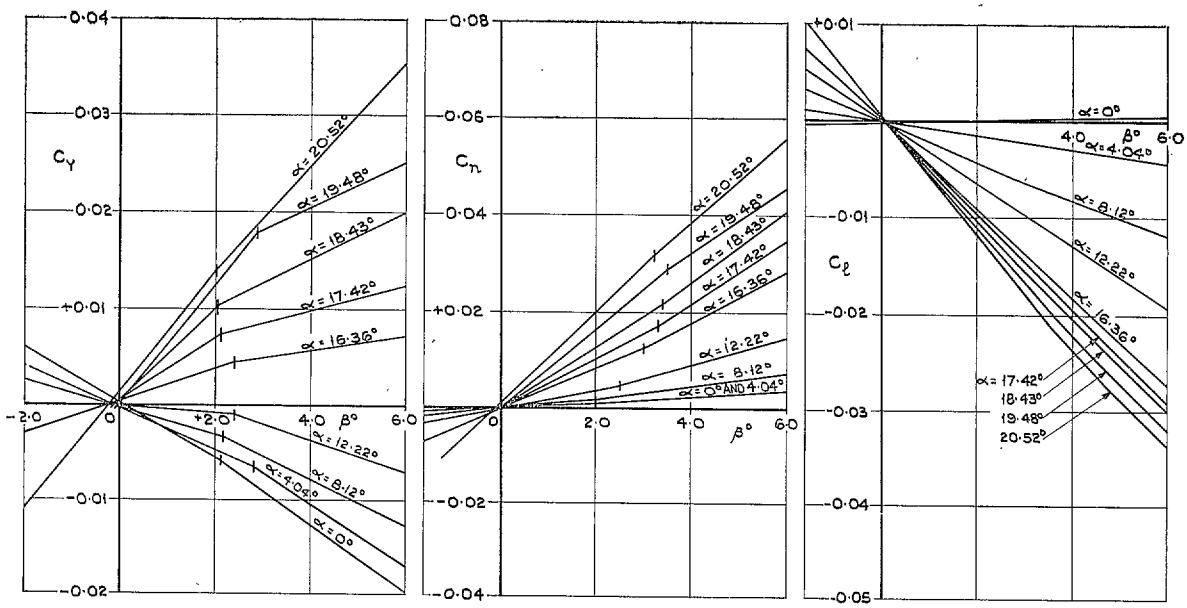

FIG. 64. Variation of C_Y, C_n and C_l with β at $M = 0{\cdot}3$, $R = 2 \times 10^6$ per ft; basic nose, with fin.

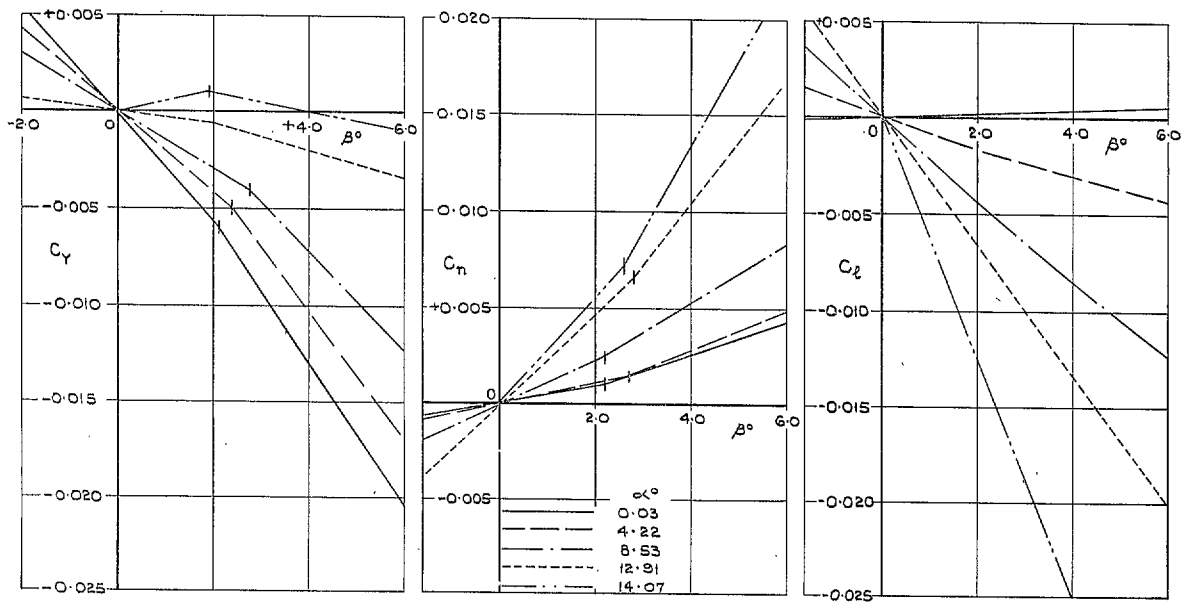

FIG. 65. Variation of C_Y, C_n and C_l with β at $M = 0{\cdot}3$, $R = 8 \times 10^6$ per ft; basic nose, with fin.

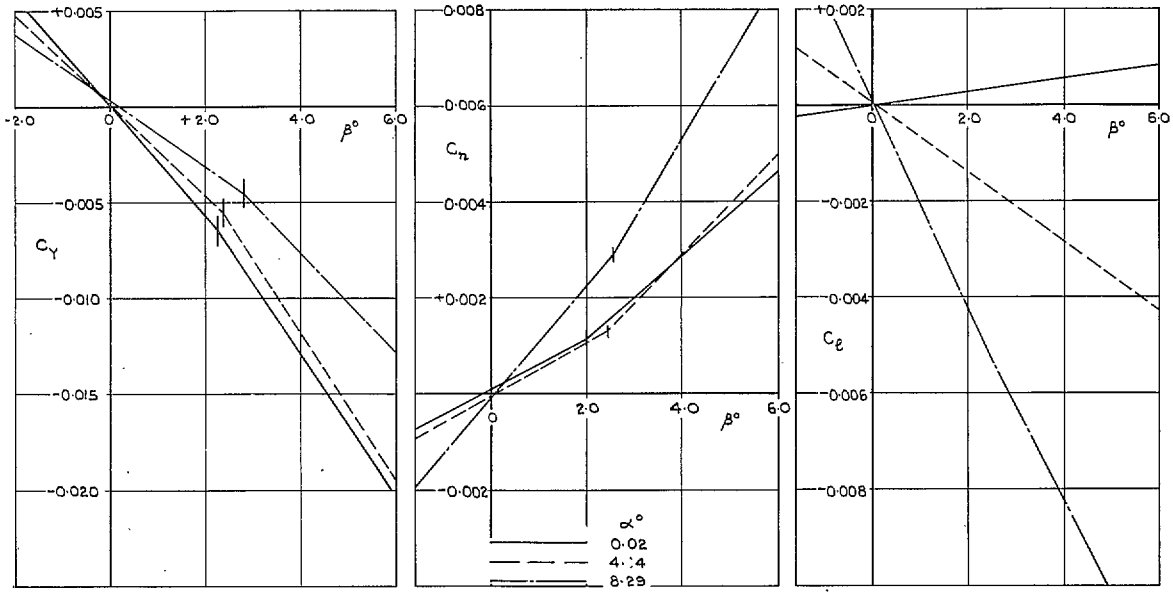

FIG. 66. Variation of C_Y, C_n and C_l with β at $M = 0{\cdot}8$; basic nose, with fin.

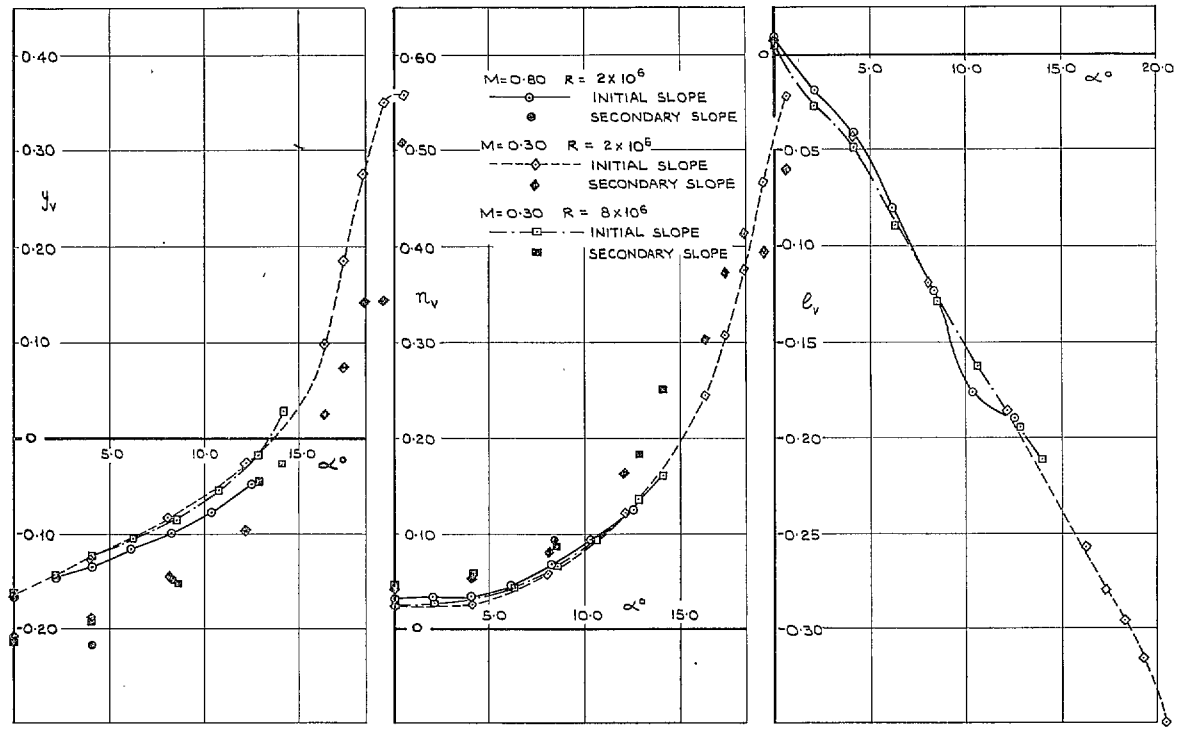

FIG. 67. Variation of y_v, n_v and l_v with α at subsonic speeds; basic nose, with fin.

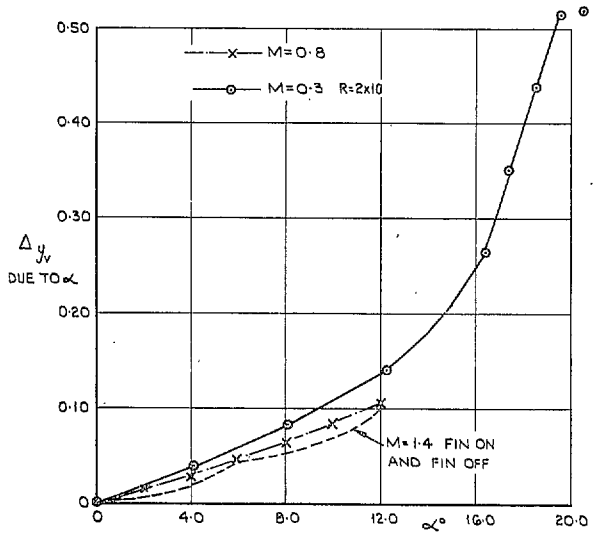

FIG. 68. Incidence dependent y_v ; subsonic speeds, basic nose, with fin.

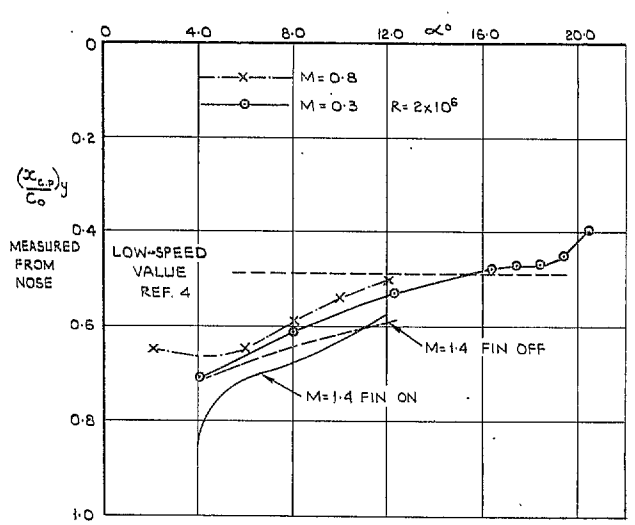

FIG. 69. Chordwise centre-of-pressure position of incidence dependent y_v ; subsonic speeds, basic nose, with fin.

(90746) Wt. 66/2301 K5 2/65. Hw.

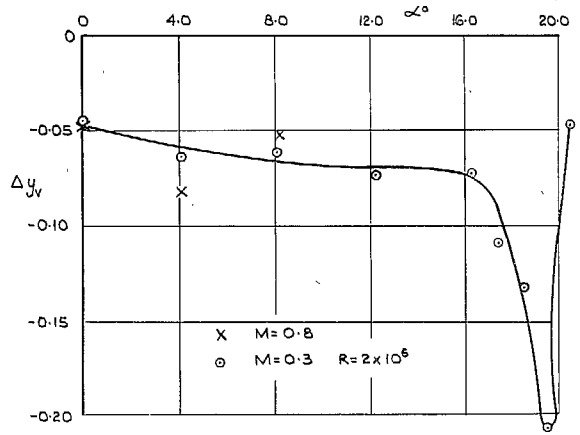

FIG. 70. Sideslip dependent y_v (secondary y_v − initial y_v); basic nose, with fin, subsonic speeds.

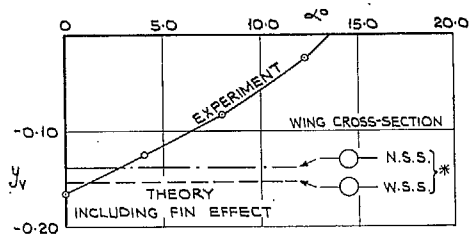

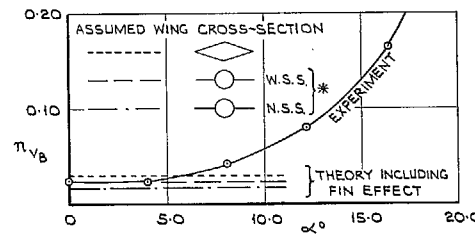

* W.S.S. – WITH STING SHROUD
N.S.S. – NO STING SHROUD

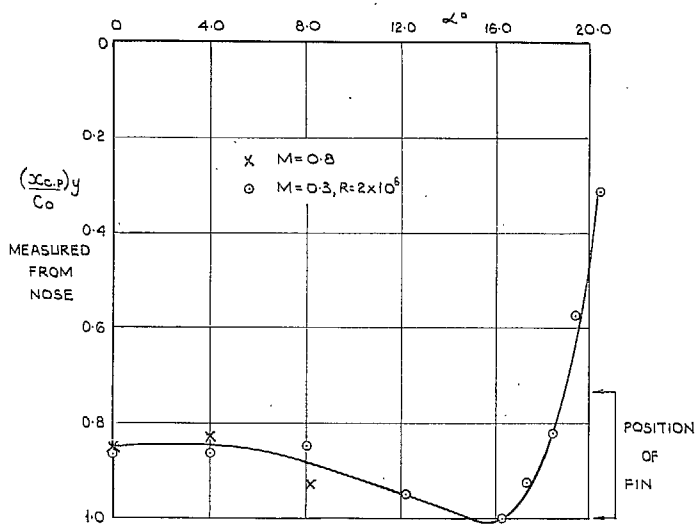

FIG. 71. Chordwise centre-of-pressure position of sideslip dependent y_v; basic nose, with fin, subsonic speeds.

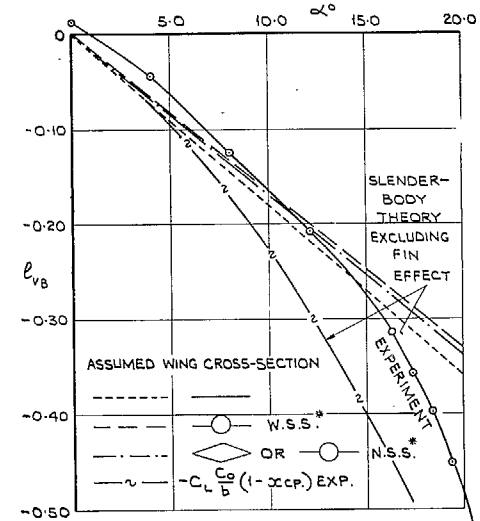

FIG. 72. Comparison with theory; y_v, $n_{v\,B}$ and $l_{v\,B}$ at $M = 0{\cdot}3$, basic nose with fin.

Publications of the Aeronautical Research Council

ANNUAL TECHNICAL REPORTS OF THE AERONAUTICAL RESEARCH COUNCIL (BOUND VOLUMES)

1945 Vol. I. Aero and Hydrodynamics, Aerofoils. £6 10*s*. (£6 13*s*. 6*d*.)
Vol. II. Aircraft, Airscrews, Controls. £6 10*s*. (£6 13*s*. 6*d*.)
Vol. III. Flutter and Vibration, Instruments, Miscellaneous, Parachutes, Plates and Panels, Propulsion. £6 10*s*. (£6 13*s*. 6*d*.)
Vol. IV. Stability, Structures, Wind Tunnels, Wind Tunnel Technique. £6 10*s*. (£6 13*s*. 3*d*.)

1946 Vol. I. Accidents, Aerodynamics, Aerofoils and Hydrofoils. £8 8*s*. (£8 11*s*. 9*d*.)
Vol. II. Airscrews, Cabin Cooling, Chemical Hazards, Controls, Flames, Flutter, Helicopters, Instruments and Instrumentation, Interference, Jets, Miscellaneous, Parachutes. £8 8*s*. (£8 11*s*. 3*d*.)
Vol. III. Performance, Propulsion, Seaplanes, Stability, Structures, Wind Tunnels. £8 8*s*. (£8 11*s*. 6*d*.)

1947 Vol. I. Aerodynamics, Aerofoils, Aircraft. £8 8*s*. (£8 11*s*. 9*d*.)
Vol. II. Airscrews and Rotors, Controls, Flutter, Materials, Miscellaneous, Parachutes, Propulsion, Seaplanes, Stability, Structures, Take-off and Landing. £8 8*s*. (£8 11*s*. 9*d*.)

1948 Vol. I. Aerodynamics, Aerofoils, Aircraft, Airscrews, Controls, Flutter and Vibration, Helicopters, Instruments, Propulsion, Seaplane, Stability, Structures, Wind Tunnels. £6 10*s*. (£6 13*s*. 3*d*.)
Vol. II. Aerodynamics, Aerofoils, Aircraft, Airscrews, Controls, Flutter and Vibration, Helicopters, Instruments, Propulsion, Seaplane, Stability, Structures, Wind Tunnels. £5 10*s*. (£5 13*s*. 3*d*.)

1949 Vol. I. Aerodynamics, Aerofoils. £5 10*s*. (£5 13*s*. 3*d*.)
Vol. II. Aircraft, Controls, Flutter and Vibration, Helicopters, Instruments, Materials, Seaplanes, Structures, Wind Tunnels. £5 10*s*. (£5 13*s*.)

1950 Vol. I. Aerodynamics, Aerofoils, Aircraft. £5 12*s*. 6*d*. (£5 16*s*.)
Vol. II. Apparatus, Flutter and Vibration, Meteorology, Panels, Performance, Rotorcraft, Seaplanes. £4 (£4 3*s*.)
Vol. III. Stability and Control, Structures, Thermodynamics, Visual Aids, Wind Tunnels. £4 (£4 2*s*. 9*d*.)

1951 Vol. I. Aerodynamics, Aerofoils. £6 10*s*. (£6 13*s*. 3*d*.)
Vol. II. Compressors and Turbines, Flutter, Instruments, Mathematics, Ropes, Rotorcraft, Stability and Control, Structures, Wind Tunnels. £5 10*s*. (£5 13*s*. 3*d*.)

1952 Vol. I. Aerodynamics, Aerofoils. £8 8*s*. (£8 11*s*. 3*d*.)
Vol. II. Aircraft, Bodies, Compressors, Controls, Equipment, Flutter and Oscillation, Rotorcraft, Seaplanes, Structures. £5 10*s*. (£5 13*s*.)

1953 Vol. I. Aerodynamics, Aerofoils and Wings, Aircraft, Compressors and Turbines, Controls. £6 (£6 3*s*. 3*d*.)
Vol. II. Flutter and Oscillation, Gusts, Helicopters, Performance, Seaplanes, Stability, Structures, Thermodynamics, Turbulence. £5 5*s*. (£5 8*s*. 3*d*.)

1954 Aero and Hydrodynamics, Aerofoils, Arrester gear, Compressors and Turbines, Flutter, Materials, Performance, Rotorcraft, Stability and Control, Structures. £7 7*s*. (£7 10*s*. 6*d*.)

Special Volumes

Vol. I. Aero and Hydrodynamics, Aerofoils, Controls, Flutter, Kites, Parachutes, Performance, Propulsion, Stability. £6 6*s*. (£6 9*s*.)
Vol. II. Aero and Hydrodynamics, Aerofoils, Airscrews, Controls, Flutter, Materials, Miscellaneous, Parachutes, Propulsion, Stability, Structures. £7 7*s*. (£7 10*s*.)
Vol. III. Aero and Hydrodynamics, Aerofoils, Airscrews, Controls, Flutter, Kites, Miscellaneous, Parachutes, Propulsion, Seaplanes, Stability, Structures, Test Equipment. £9 9*s*. (£9 12*s*. 9*d*.)

Reviews of the Aeronautical Research Council

1949–54 5*s*. (5*s*. 5*d*.)

Index to all Reports and Memoranda published in the Annual Technical Reports

1909–1947 R. & M. 2600 (out of print)

Indexes to the Reports and Memoranda of the Aeronautical Research Council

Between Nos. 2451–2549: R. & M. No. 2550 2*s*. 6*d*. (2*s*. 9*d*.); Between Nos. 2651–2749: R. & M. No. 2750 2*s*. 6*d*. (2*s*. 9*d*.); Between Nos. 2751–2849: R. & M. No. 2850 2*s*. 6*d*. (2*s*. 9*d*.); Between Nos. 2851–2949: R. & M. No. 2950 3*s*. (3*s*. 3*d*.); Between Nos. 2951–3049: R. & M. No. 3050 3*s*. 6*d*. (3*s*. 9*d*.); Between Nos. 3051–3149: R. & M. No. 3150 3*s*. 6*d*. (3*s*. 9*d*.); Between Nos. 3151–3249: R. & M. No. 3250 3*s*. 6*d*. (3*s*. 9*d*.); Between Nos. 3251–3349: R. & M. No. 3350 3*s*. 6*d*. (3*s*. 10*d*.)

Prices in brackets include postage

Government publications can be purchased over the counter or by post from the Government Bookshops in London, Edinburgh, Cardiff, Belfast, Manchester, Birmingham and Bristol, or through any bookseller

Printed and published by
HER MAJESTY'S STATIONERY OFFICE

To be purchased from
York House, Kingsway, London W.C.2
423 Oxford Street, London W.1
13A Castle Street, Edinburgh 2
109 St. Mary Street, Cardiff
39 King Street, Manchester 2
50 Fairfax Street, Bristol 1
35 Smallbrook, Ringway, Birmingham 5
80 Chichester Street, Belfast 1
or through any bookseller

Printed in England

S.O. Code No. 23-3390